

# Variability of transit light curves of *Kepler* objects of interest

O. V. Arkhypov<sup>1</sup>, M. L. Khodachenko<sup>1,2,3</sup>, and A. Hanslmeier<sup>4</sup>

<sup>1</sup> Space Research Institute (IWF), Austrian Academy of Sciences, Schmiedlstrasse 6, 8042 Graz, Austria  
e-mail: [oleksiy.arkhypov@oeaw.ac.at](mailto:oleksiy.arkhypov@oeaw.ac.at); [maxim.khodachenko@oeaw.ac.at](mailto:maxim.khodachenko@oeaw.ac.at)

<sup>2</sup> Skobeltsyn Institute of Nuclear Physics, Moscow State University, 119992 Moscow, Russia

<sup>3</sup> Institute of Astronomy of the Russian Academy of Sciences, 119017 Moscow, Russia

<sup>4</sup> Institute of Physics, Karl-Franzens University of Graz, Universitätsplatz 5, 8010 Graz, Austria  
e-mail: [arnold.hanslmeier@uni-graz.at](mailto:arnold.hanslmeier@uni-graz.at)

Received 12 December 2019 / Accepted 26 April 2020

## ABSTRACT

**Context.** Hitherto, the study of exoplanetary transit timing and duration variability has supposed transit light curves (TLCs) to be symmetric, suggesting a priori a spherical shape for the transiting object, for example, an exoplanet. As a result, the independent positions of transit borders are unknown. However, the borders of TLCs are most sensitive to the presence of exo-rings and/or dust formations of great interest.

**Aims.** For the first time we check for a timing variability of independently treated borders of transits of different types of exoplanets.

**Methods.** Using quadratic approximation for the start-, end-, and minimum parts of the long-cadence TLCs from the *Kepler* mission archive after their whitening and phase folding, we find the corresponding transit border timings:  $\Delta t_s$ ,  $\Delta t_e$ , respectively, and the TLC minimum time  $\Delta t_m$ . These parameters were found separately for each folded TLC constructed in the consequent non-overlapping time-windows with the respective medium time  $t_w$ . Temporal and cross-correlation analysis of the obtained series of  $\Delta t_s(t_w)$ ,  $\Delta t_e(t_w)$ , and  $\Delta t_m(t_w)$  were applied for the detection and diagnostics of variability of transit borders and TLC asymmetry.

**Results.** Among the considered TLCs of 98 *Kepler* objects of interest (KOIs), 15 confirmed giant exoplanets and 5 objects with still debatable status (probably non-planets) show variations in their transit timing parameters at timescales from  $\approx 400$  to  $\geq 1500$  days. These variations are especially well manifested as an anti-correlation between  $\Delta t_s$  and  $\Delta t_e$ , indicating variability in the dimensions of transiting shadows, especially along their trajectories. There are also objects with well pronounced oscillations of transit border timing and asymmetry.

**Conclusions.** The discovered variability of transit timing is important as an indicator of large-scale non-stationary processes in the atmospheres of KOIs, as well as dust and aerosol generation in their upper layers and in their close vicinity. These findings highlight the need for a dedicated and detailed study.

**Key words.** planets and satellites: general – planets and satellites: rings – planet-star interactions

## 1. Introduction

Hitherto, studies of the variability of exoplanetary transit timings (i.e., start/end time and duration) have supposed the form of transit light curves (TLCs) to be symmetric, suggesting a spherical exoplanet (e.g., [Holczer et al. 2016](#)). As a result, the independent positions of transit borders are unknown. Furthermore, the borders of the TLC are most sensitive to the shape of the transiting object, which is affected by possible presence of exo-rings. ([Schlichting & Chang 2011](#)) and dust formations ([Arkhypov et al. 2019](#); [Wang & Dai 2019](#)).

In particular, the variable stellar ionizing radiation could vary the effective size of the shadow of an exoplanet with outflowing ([Wang & Dai 2019](#)), apparently dusty ([Arkhypov et al. 2019](#)) atmosphere. A circumplanetary disk of dusty plasma, formed in some cases ([Khodachenko et al. 2015](#)), could also affect the planetary shadow, resulting in variation of its effective size due to reconnection events in the disk. Another mechanism causing variability in transits may be related with shocks and material flows around hot Jupiters ([Llama et al. 2013](#)). All these factors, as well as precessing exo-rings, might result in variability in transit borders. Here, we therefore perform independent measurements of transit border timings and TLC minimum time and investigate variations thereof.

In that respect, TLCs provided by the *Kepler* space telescope appear to be a promising but still superficially studied source of information concerning possible variability in exoplanetary transits. So far, such variability has only been studied for decaying rocky planets ([Sanchis-Ojeda et al. 2015](#); [Garai 2018](#) and therein) and asteroids ([Rappaport et al. 2016](#) and therein). In this paper, we analyze for the first time the TLC variability of different types of transiting *Kepler* objects of interest (KOIs). The maximal duration of available data records and their high precision make *Kepler* data the best choice to search for tenuous signatures of variability in TLCs.

For the analysis we apply a specially elaborated method, which is explained in Sect. 2. The obtained results are described in Sect. 3, discussed in Sect. 4, and concluded in Sect. 5.

## 2. Method and stellar set

### 2.1. Transit light curve analysis

We use publicly available light curves from the *Kepler* mission (NASA Exoplanet Archive, thereafter NASA EA<sup>1</sup>), after pre-search data conditioning (light flux  $F_{\text{PDC}}$  hereinafter), where

<sup>1</sup> <https://exoplanetarchive.ipac.caltech.edu/>

instrumental drifts, focus changes, and thermal transients are removed or suppressed (Jenkins et al. 2010). Our survey relies on long-cadence data with a photon accumulation (i.e., exposure) period of  $\delta t_L = 29.4$  min, or 0.02 days. This approach provides the highest precision of the input TLCs, although it cannot resolve the details of ingress and egress parts. The short-cadence data with an exposure period of  $\delta t_S = 1$  min, in spite of a higher time resolution, are available for a lesser number of stars and not for all quarters; and they also increase the photometry error due to photon noise by a factor of  $\sqrt{\delta t_L/\delta t_S} = 5.4$ .

To prepare the analyzed light curves for determining TLC timing parameters we first remove the residual instrumental drifts as well as the stellar variability at timescales longer than the transit duration  $\Delta t_{tr}$ , taken from the NASA EA. This procedure consists of the following steps: (a) Extraction of a fragment of light curve, enclosed within a time interval of  $\pm 10\Delta t_{tr}$  centered at the particular transit (see Fig. 1a). (b) Normalization of the extracted fragment:  $F_{PDC}/\langle F_{PDC} \rangle$ , where  $\langle F_{PDC} \rangle$  means an average flux over the light-curve fragment. (c) Removal of the transit from the analyzed light-curve fragment, including the half-exposition margins of  $\pm 0.01$  days, based on the published transit duration values (NASA EA). (d) Approximation of the remaining light-curve fragment without transit with a sixth-order polynomial:  $F_b(t) = at^6 + bt^5 + ct^4 + dt^3 + et^2 + ft + g$ , where  $t$  is the time of flux measurement, and  $a, b, c, d, e, f, g$  are the fitted coefficients. This approximation is an iterative process (ten iterations), with consequent exclusion of remaining stellar flares, light-curve artifacts, and residual transit effects above the threshold  $|(F_{PDC}(t)/\langle F_{PDC}(t) \rangle) - F_b(t)| > 3\sigma_b$ , where  $\sigma_b$  is a standard deviation from the approximation  $F_b(t)$ . Since the final approximation  $F_b(t)$  is insensitive to the transit (Fig. 1a), we consider it as a reference level with which to determine the flux decrease during the transit:  $\Delta F_k = [F_{PDC}(t)/\langle F_{PDC}(t) \rangle] - F_b(t)$ , which is used in the analyses below.

In the long-cadence data records with the above-mentioned time step  $\delta t_L$ , there are only a few flux measurement points  $n = \Delta t_{tr}/\delta t_L \sim 5$  on the time interval of transit duration with a typical value of  $\Delta t_{tr} \sim 0.1$  day. This is insufficient for our study of the transit border timing. We therefore increased the number of data points up to  $K = N\Delta t_{tr}/\delta t_L \sim 100$  by combining the measurements of  $N = \Delta t_w/P_{tr}$  transits within a time-window of width  $\Delta t_w$  centered at  $t_w$  into one phase-folded TLC  $\Delta F(\Delta t)$ . Here,  $\Delta t \equiv t - t_E$  is the time counted for each transit with number  $E = 0, 1, 2, \dots$  relative to its mid-time  $t_E = t_0 + P_{tr}E$ . The reference transit time  $t_0$  and the transit period  $P_{tr}$  are taken in their cumulative versions from the NASA EA. The used time-windows are defined as a sequence of adjacent frames, so that  $t_w = t_0 + \Delta t_w J_w$ , where  $J_w = 0, 1, 2, \dots$  is the number of a particular time-window.

The creation of a folded TLC by combining individual transits within a window is also an iterative process aimed at exclusion of light-curve artifacts, stellar flares, and starspot eclipses. In order to clean the analyzed TLC of outliers related with the above-mentioned effects, we approximate it with a fourth-order polynomial  $\Delta F \approx \Delta F_{ap}(\Delta t) = a_{ap}(\Delta t)^4 + b_{ap}(\Delta t)^3 + c_{ap}(\Delta t)^2 + d_{ap}\Delta t + e_{ap}$ , where  $a_{ap}, b_{ap}, c_{ap}, d_{ap}$  and  $e_{ap}$  are the fitted coefficients. All the flux values with  $|\Delta F(\Delta t) - \Delta F_{ap}(\Delta t)| > 3\sigma_{ap}$  are excluded from further consideration and the whole approximation procedure is repeated with a new estimate for  $\sigma_{ap}$  in order to remove another group of outliers in the TLC. After ten rounds of such iterations, the final folded TLC is sufficiently smooth for further analysis. An example of such a folded and iteratively smoothed TLC is shown in Fig. 1b.

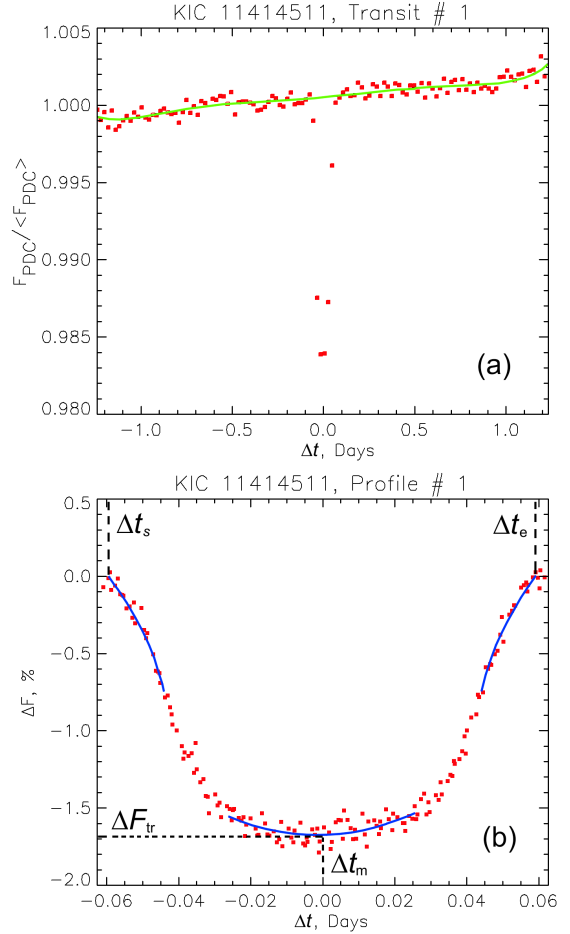


**Fig. 1.** Example of light-curve processing (the star KIC 11414511). *Panel a:* approximation of the transit background (red squares) with a sixth-order polynomial  $F_b(t)$  (green curve). *Panel b:* folded profile  $\Delta F(\Delta t)$  of 25 adjacent individual transits. Blue curves are the applied polynomial approximations used for measurements of labeled parameters.

For the correlation analysis it is important to provide an acceptable number ( $\geq 3$ ) of phase-folded TLCs (i.e., the number of time-windows  $N_w$  over the whole available *Kepler* data record of about 4 yr), whilst keeping a sufficient number of flux measurement points in each folded TLC,  $K$ , for the transit borders study. We note that, in the case of short transit periods ( $P_{tr} \lesssim 10$  days), the value of  $K$  can be easily kept up to 200, whereas for intermediate ( $10 \lesssim P_{tr} \lesssim 20$  days) and long ( $P_{tr} \gtrsim 20$  days) periods the number  $K$  was decreased to 100 and 60, respectively. These values were adopted in the regular survey of the whole target list in Sects. 3.1 and 3.2, whereas during the analysis of particular objects in Sect. 3.3 the window parameter  $N$  has been additionally varied to optimize the time resolution for optimal visualization of the transit variability.

To determine the parameters of a TLC with high accuracy, we separately approximate the start-, end-, and minimum- parts of the obtained folded TLCs with second-order polynomials. In particular, the minimum-part of the TLC is approximated as  $\Delta F \approx F_a = g\Delta t^2 + h\Delta t + q$  within the interval  $|\Delta t| < \Delta t_{tr}/4$  centered at the folded TLC mid-time ( $\Delta t = 0$ ). An additional reason for using the second-order polynomial here is to avoid the uncertainty associated with selection among multiple extremes, which are typical for higher-order polynomial approximations. Moreover, the single minimum at  $\Delta t_m = -h/(2g)$  is considered also

as the TLC minimum-time, which depends mainly on the stellar limb darkening. This method reduces the sensitivity of the TLC timing parameter  $\Delta t_m$  to possible local minima caused by starspots. Correspondingly, the depth of the TLC minimum can be found as  $\Delta F_{tr} = g\Delta t_m^2 + h\Delta t_m + q$ .

For the determination of TLC border timing parameters, that is, its start and end time moments, indicated with the indexes “s” and “e”, respectively, we use second-order polynomial approximations of the reverse dependence  $\Delta t(\Delta F) = a_{s,e}\Delta F^2 + b_{s,e}\Delta F + c_{s,e}$  within the interval  $0.5\Delta F_{tr} < \Delta F < 0$  separately for the start- and end- parts of the TLC (i.e., indexes “s” or “e”, respectively). Correspondingly, two different ranges of  $\Delta t$ , namely (i)  $-\Delta t_{tr}/2 - \delta t_L/2 < \Delta t < 0$  and (ii)  $0 < \Delta t < \Delta t_{tr}/2 + \delta t_L/2$ , are considered (see in Fig. 1b). We note that the above specified ranges for the  $\Delta F$  and  $\Delta t$  are jointly used for the extraction of flux count points involved in the approximations of TLC start- and end-parts. As the transit border must be located at  $\Delta F = 0$ , the approximation polynomial coefficient  $c_{s,e}$  directly gives the border times  $\Delta t_s = c_s$  and  $\Delta t_e = c_e$  of the folded TLC defined within a particular time-window centered at a certain  $t_w$ . To study variability of the parameters  $\Delta F_{tr}$ ,  $\Delta t_m$ ,  $\Delta t_s$ , and  $\Delta t_e$ , we similarly associate them with the corresponding central time  $t_w$  of the time-window for which the folded TLC was obtained. The standard errors of  $\Delta F_{tr}$ ,  $\Delta t_m$ ,  $\Delta t_s$  and  $\Delta t_e$  (Fig. 2) are expressed in terms of the definition errors of the coefficients of the approximating polynomials.

As the quadratic approximations of TLC border parts are the simplest ones, they also provide an acceptable fit for the transit border regions of interest above the inflection point (Fig. 1b). The cubic and higher order polynomials increase the dispersion of  $\Delta t_s$  and  $\Delta t_e$  times defined for different time-windows, i.e., windows with different  $J_w$ . Although the polynomial method could result in systematic errors in the defining of  $\Delta t_s$  and  $\Delta t_e$ , such regular displacements do not affect the detection of transit variability. Further below, the transit shape parameter  $A_s = (\Delta t_m - \Delta t_s)/(\Delta t_e - \Delta t_s)$  and the Pearson correlation coefficients  $r_{se}$  between  $\Delta t_s$  and  $\Delta t_e$ , as well as analogous cross-correlations  $r_{me}$  (between  $\Delta t_m$  and  $\Delta t_e$ ),  $r_{ms}$  (between  $\Delta t_m$  and  $\Delta t_s$ ),  $r_{As}$  (between  $A_s$  and  $\Delta t_s$ ),  $r_{Ae}$  (between  $A_s$  and  $\Delta t_e$ ) and  $r_{Am}$  (between  $A_s$  and  $\Delta t_m$ ), are used for the phenomenological analysis of the folded TLCs.

## 2.2. Compiled data set

The considered data set of 98 KOIs and the results obtained for these are presented in Table A.1. Our targets were selected among the most qualitatively observed objects from the list by Aizawa et al. (2018) and supplemented by other *Kepler* transiting bodies, for which only long-cadence light curves are available, but with high signal-to-noise ratios ( $S/N \gtrsim 1000$ ) according to NASA EA. To avoid the inter-transit interference in multi-planetary systems, only the cases with single transiting object (i.e., transiter) were included in our target list.

The KOIs with current false positive status were not considered, apart from KOI 125.01, KOI 631.01, and KOI 1416.01, which were reclassified as false positives already after the compilation of our data set. The status of these objects is marked in Table A.1 with “n”, that is, probable non-planets. The same mark is assigned to KOI 823.01, KOI 971.01, KOI 1154.01, KOI 6085.01 and KOI 6774.01 which have unknown masses and anomalously high radii,  $R_p > 24 R_e$  (here  $R_e$  stays for the radius of Earth), exceeding the empirical range of the radius–mass relation (see Fig. 1 in Ulmer-Moll et al. 2019). Altogether, the highest status “p!” of confirmed exoplanets with measured

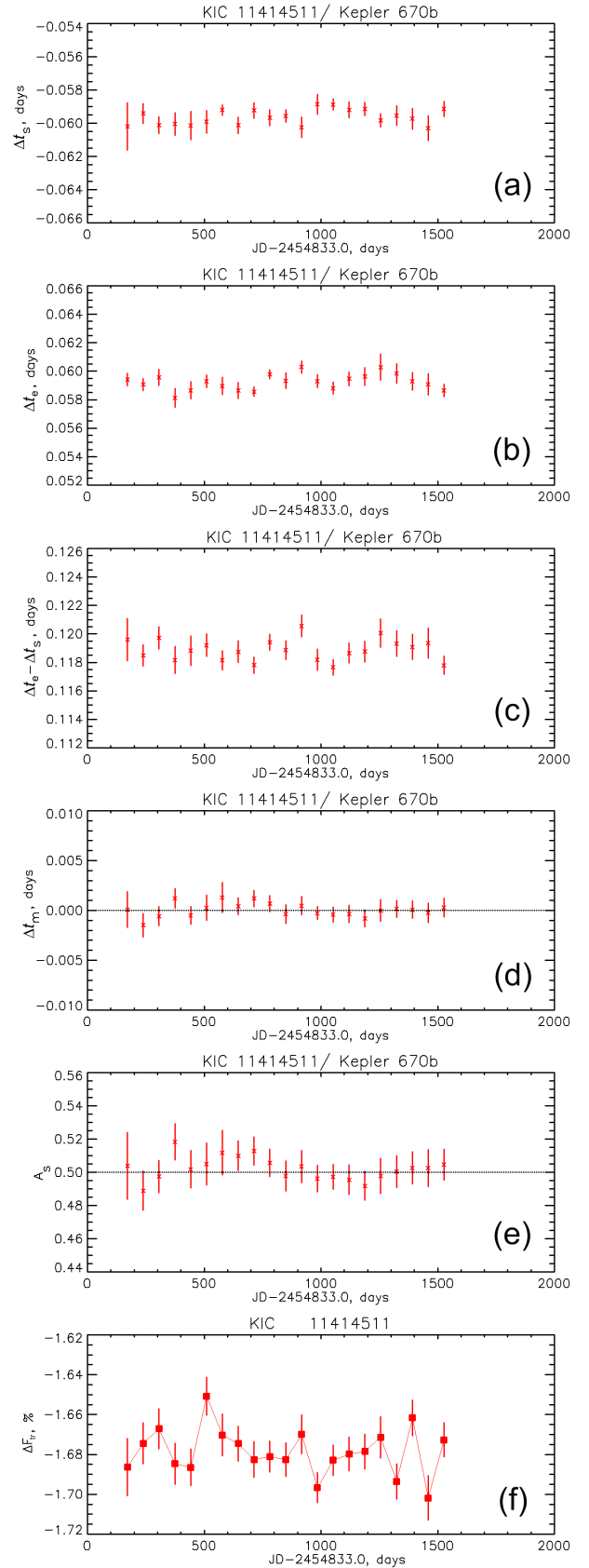


**Fig. 2.** Temporal behavior of the transit timing parameters of real TLCs like in Fig. 1b, compiled for a sequence of adjacent time-windows, vs. time in Julian days JD: *panel a*: transit start-time  $\Delta t_s$ , *panel b*: transit end-time  $\Delta t_e$ , *panel c*: transit duration  $\Delta t_e - \Delta t_s$ , *panel d*: transit minimum-time  $\Delta t_m$  (maximal flux decrease), *panel e*: transit shape parameter  $A_s$ , *panel f*: transit flux decrease  $\Delta F_{tr}$ .

masses below  $13 M_J$  (here  $M_J$  stays for the mass of Jupiter) is assigned to 40% of the objects in the considered set of 98 KOIs. One other object, KOI 680.01, was also given the status “p!”. This is a so-called super-puff which has an obviously planetary mass of  $0.84 \pm 0.15 M_J$  (Almenara et al. 2015), in spite of a relatively large radius  $R_p = 26.5^{+3.6}_{-9.4} R_e$ . Confirmed planets with unknown masses are marked with “p” (35% of cases), whereas unconfirmed candidates were given the status index “c” (17%). To check the status of objects, we additionally used the Extrasolar Planets Encyclopedia<sup>2</sup> and the SIMBAD Astronomical Database<sup>3</sup>. The objects for which the previously suggested false-positive or stellar eclipse status has been canceled in NASA EA are marked with the sign “?” in our Table A.1. Finally, the status mark “\*” signifies that the KOI formally has the current flag of stellar eclipse false positive, but the measured mass of the object contradicts its assumed stellar nature.

There is a special notation in the KOI cumulative list of NASA EA for KOIs “that are observed to have a significant secondary event (i.e., the secondary TLC minimum due to the eclipse of the planet by the star), transit shape, or out-of-eclipse variability” indicating that the transit-like event is most likely caused by an eclipsing binary. “However, self-luminous, hot Jupiters with a visible secondary eclipse will also have this flag set, but with a disposition of PC (i.e., planetary candidate)”.

For example, in our set, the objects KOI 13.01 and KOI 18.01 (Kepler-13b and -5b) orbiting the stars KIC 9941662 and KIC 8191672, respectively, have the stellar eclipse false positive flag in the KOI cumulative list of NASA EA. Nevertheless, the measurements of their masses by two different methods give non-stellar values (Esteves et al. 2013) corresponding to the classification of objects as confirmed planets in the same NASA EA. As to the secondary eclipses, they are an important instrument of exoplanet meteorology used in many dedicated studies of genuine hot Jupiters (e.g., Jackson et al. 2019; Pass et al. 2019).

The presence in our data set of the admixture (8%) of objects with the supposed non-planetary status “n” is motivated by the fact that non-planetary KOIs need to be studied as well as exoplanets. Furthermore, the false-positive status is a probabilistic issue (e.g., Morton et al. 2016) and for some objects it changes from one catalog to another. Hence, the current false-positive status of an object does not completely exclude a planetary nature.

Figure 3 demonstrates the ranges of physical parameters (radius  $R_p$  of the transiting body and its orbit radius  $a_p$ ) of the KOIs in the analyzed data set. One can see that our target list includes mainly hot Jupiters with an admixture of hot neptunes and super-earths as well as KOI 823.01 and KOI 971.01 of stellar size, classified as planetary “candidates” in the *Kepler* data of NASA EA. In the case of KOI 1478.01 at KIC 12403119 with maximal  $P_{tr} = 76.13$  days, which appeared in a kind of resonance with the flux counting period, the parameters  $\Delta t_s$ ,  $\Delta t_m$  and  $\Delta t_e$  were found only in two time-windows. This always gives an exact formal correlation, that is,  $r_{se} = \pm 1$ . Such fictive correlations were excluded from Table A.1.

### 3. Results and their analysis

Table A.1 shows the main results from processing the compiled data set, including the standard deviations  $\sigma_m$ ,  $\sigma_s$  and  $\sigma_e$  of transit timings  $\Delta t_m$ ,  $\Delta t_s$ , and  $\Delta t_e$ , respectively, as well as the timing cross-correlations  $r_{ms}$ ,  $r_{me}$ , and  $r_{se}$  and the average transit shape

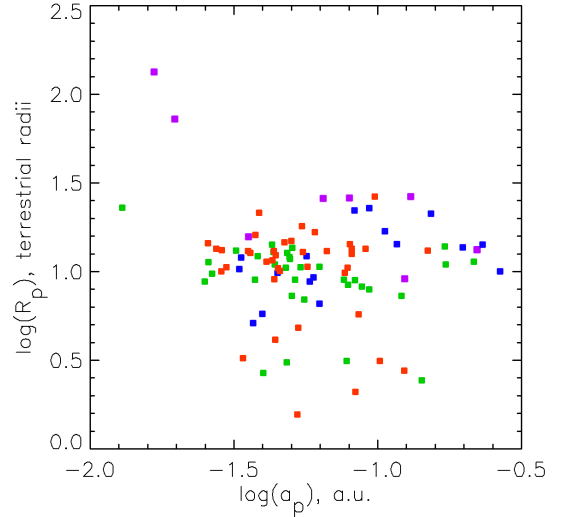


**Fig. 3.** Distribution of selected KOI targets (listed in Table A.1) vs. the radii  $R_p$  and orbital semimajor axes  $a_p$  of transitors according to NASA EA<sup>4</sup>. Color shows the status of objects: violet – probably non-planets (“n” in Table A.1); blue – candidates (“c” in Table A.1); green – confirmed planets but with unknown masses (“p” in Table A.1); red – confirmed planets with measured planetary masses (“p!” in Table A.1). The cases with “\*” and “?” are included. The same color coding is used throughout the paper.

parameter  $\langle A_s \rangle$  (see Sect. 2.1 for details). Despite the dispersed errors, Table A.1 contains hidden patterns which enable certain interpretations and conclusions. Below we present some examples of our findings after processing the results, including general statistics, and we highlight several specific individual cases.

#### 3.1. Transit light curve border timing variability

Figure 2 shows some typical examples of the temporal behavior of the obtained transit timing parameters  $\Delta t_s$ ,  $\Delta t_m$ ,  $\Delta t_e$ , and  $\Delta F_{tr}$ , as well as of their combinations ( $\Delta t_e - \Delta t_s$  and  $A_s$ ). We use the following three formal criteria for the detection of the best cases of transit border timing variability:

(a) For  $\Delta t_s$ , the ratio  $\sigma_s/\varepsilon_s > 2.5$  holds true, where  $\sigma_s$  is the standard deviation of the estimate of  $\Delta t_s$  over the time-windows, and  $\varepsilon_s$  is an error of  $\Delta t_s$  measurements averaged over all time-windows.

(b) For  $\Delta t_e$ , the same criterion as for  $\Delta t_s$  is considered, that is,  $\sigma_e/\varepsilon_e > 2.5$ .

(c) For  $r_{se}$ , significant cross-correlation  $|r_{se}|/\sigma_{rse} > 2.5$  is required, where  $\sigma_{rse} = (1 - r_{se}^2)/\sqrt{N_w - 1}$  is a standard error of  $r_{se}$  according to Hotelling (1953), and  $N_w$  is the number of time-windows in which the phase-folded TLCs are generated.

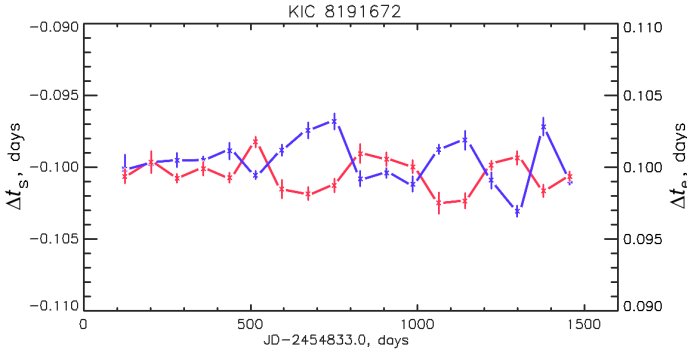
If any of these criteria hold true, the KOI is considered as potentially interesting. An additional condition of  $N_w \geq 10$  was applied to define the best tracked cases. The results of such a selection are presented in Table A.2.

Figure 4 shows an example of varying transit border timing for KOI 18.01 in the light curve of KIC 8191672 from Table A.2. The plots of  $\Delta t_s$  and  $\Delta t_e$  versus time are combined to demonstrate their clear anti-correlation  $r_{se} = -0.73 \pm 0.11$ . All 17 KOIs in Table A.2 show analogous ( $r_{se} \leq -0.51$ ) negative cross-correlation. Supposing a stable host star (i.e., with a constant radius), such an anti-correlation effect can have two explanations: (1) a varying impact parameter  $\beta$  of the transiting body

<sup>2</sup> <http://exoplanet.eu>

<sup>3</sup> <http://simbad.u-strasbg.fr>

<sup>4</sup> <https://exoplanetarchive.ipac.caltech.edu/>



**Fig. 4.** Anti-correlated variations of  $\Delta t_s$  (red) and  $\Delta t_e$  (blue) for KOI 18.01 revealed in the TLC of KIC 8191672. The measured timing values are shown as crosses with error bars.

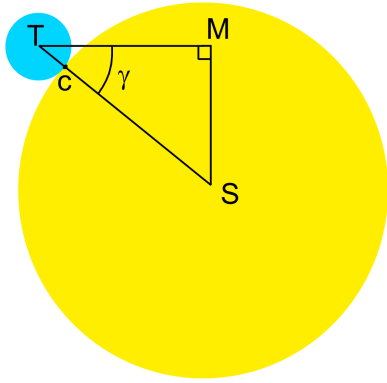


**Fig. 5.** Transit scheme. Labels “S” and “T” mark the centers of a stellar disk (yellow) and transiter’s disk (blue), respectively. The contact point “c” of the disks corresponds to the transit start (or end) time, i.e., the time moment  $\Delta t_s$  or  $\Delta t_e$ . The center of the transiting body moves along the visible trajectory from “T” to “M” (or vice versa), where “M” is the middle point of the trajectory.

(i.e., the minimal distance between the stellar disk center and the transiter’s trajectory projection on the disk, expressed in stellar radii), or (2) a varying effective size of the transiter. To distinguish between these options, let us consider their contribution to the TLC border timing.

Figure 5 shows the transit scheme used to specify the transit border times  $\Delta t_s$  or  $\Delta t_e$ . From the triangle  $\triangle TMS$ , one can express the semi-trajectory TM as  $x = \sqrt{(R_* + R_p)^2 - (\beta R_*)^2}$ , where  $R_*$  and  $R_p$ , i.e., the distances cS and cT, are the stellar and transiting planet radii, respectively. This semi-trajectory is related with the transit border timing as follows:  $|\Delta t_{s,e}| = x/V_p$ , where  $V_p = 2\pi a_p/P_{tr}$  is the velocity of a visible transiter (across the stellar disk), and  $a_p$  is the orbit radius from NASA EA. We note that we assume circular orbits, because all KOIs in our set have zero orbital eccentricities according to the “Kepler candidate overview pages” in NASA EA. Therefore, a small variation  $\Delta x$  of  $x$  can be expressed in terms of fluctuations (i.e., deviations from averaged values)  $\Delta\beta$  and  $\Delta R_p$  of the corresponding parameters:

$$\Delta x = \frac{\partial x}{\partial \beta} \Delta \beta + \frac{\partial x}{\partial R_p} \Delta R_p, \quad (1)$$

where

$$\frac{\partial x}{\partial \beta} = \frac{-\beta R_*^2}{x}, \quad (2)$$

$$\frac{\partial x}{\partial R_p} = \frac{R_* + R_p}{x}. \quad (3)$$

Let us consider the effect of only the first term in Eq. (1) expressed via standard deviations:  $\sigma_{s,e} \equiv \sqrt{\langle(\Delta x)^2\rangle}/V_p$ . Then Eqs. (1) and (2) give

$$\sigma_{s,e} = \frac{1}{V_p} \left| \frac{\partial x}{\partial \beta} \right| \sigma_\beta = \frac{\beta R_*^2}{x V_p} \sigma_\beta, \quad (4)$$

where  $\sigma_\beta \equiv \sqrt{\langle(\Delta\beta)^2\rangle}$  is the standard deviation of the impact parameter  $\beta$ . Correspondingly, for  $\beta = 0$ ,  $\sigma_{s,e} = 0$ , whereas for  $\beta \rightarrow 1$  (since  $R_p \ll R_*$ ) in view of  $x \rightarrow 0$ ,  $\sigma_{s,e} \rightarrow \infty$ . Therefore, varying impact parameter  $\beta$  should result in a maximum of  $\sigma_{s,e}$  at  $\beta \approx 1$ , which means that the KOI objects with most varying TLC border timing should have  $\beta$  close to unity.

Similarly, let us consider now the effect of the second term in Eq. (1),

$$\Delta x = \frac{\partial x}{\partial R_p} \Delta R_p = \frac{R_* + R_p}{x} \Delta R_p. \quad (5)$$

For  $R_p \ll R_*$ , we obtain from Eq. (5) the standard deviations:

$$\sigma_{s,e} \equiv \frac{\sqrt{\langle(\Delta x)^2\rangle}}{V_p} \approx \frac{R_*}{V_p \sqrt{R_*^2 - (\beta R_*)^2}} \sigma_{R_p}, \quad (6)$$

where  $\sigma_{R_p} \equiv \sqrt{\langle(\Delta R_p)^2\rangle}$  is the standard deviation of  $R_p$ . We note that, here, the values  $R_p$  and its standard deviation  $\sigma_{R_p}$  do not concern the regular planetary radius, but its “effective” value at the point where the planetary shadow has its first or last contact with the stellar limb (the point “c” in Fig. 5). This “effective radius” may depend on the orientation of the line of sight with respect to the orbit of the planet. Even for a single planet with constant shape,  $\sigma_{R_p}$  can depend on the impact parameter  $\beta$ .

Taking into account the above explanations, we differentiate Eq. (6) with respect to the parameter  $\beta$ :

$$\frac{\partial \sigma_{s,e}}{\partial \beta} \approx \beta \frac{R_*^3}{x^3 V_p} \sigma_{R_p} + \frac{R_*}{x V_p} \frac{\partial \sigma_{R_p}}{\partial \beta}. \quad (7)$$

The first term in Eq. (7) is always positive and at  $\beta \approx 1$  (i.e.,  $x \rightarrow 0$ ) it reaches its maximum, which, according to Eq. (6), also means the achieved maximal value of  $\sigma_{s,e}$ . Another maximum of  $\sigma_{s,e}$  is possible due to the second term. Its sign is controlled by the derivative  $\partial \sigma_{R_p}/\partial \beta$ . Furthermore, this derivative characterizes the shape of the transiting body because the parameter  $\beta$  is related with the position angle  $\angle MTS \equiv \gamma = \arcsin[\beta R_*/(R_* + R_p)]$  of the first (or last) contact point “c” in Fig. 5.

Figure 6a shows a histogram of  $\beta$  estimates for all KOIs from NASA EA. The narrow peak at  $\beta \approx 0$  means a likely biased coplanarity of KOI orbits with a distant observer. Therefore, when preparing the histograms in Figs. 6b and c for our set of targets (Table A.1), we exclude objects with  $\beta \lesssim 0.07$  from consideration, focusing on more realistic random distribution over  $\beta$ . In particular, the histogram in Fig. 6b constructed for the KOIs with the negative border timing cross-correlation  $r_{se} < 0$  shows a clear concentration of such objects especially those with the confirmed planet status marked by red and green colors at low values of  $\beta$ , whereas the histogram in Fig. 6c made for the objects with positive cross-correlation  $r_{se} > 0$  has a maximum

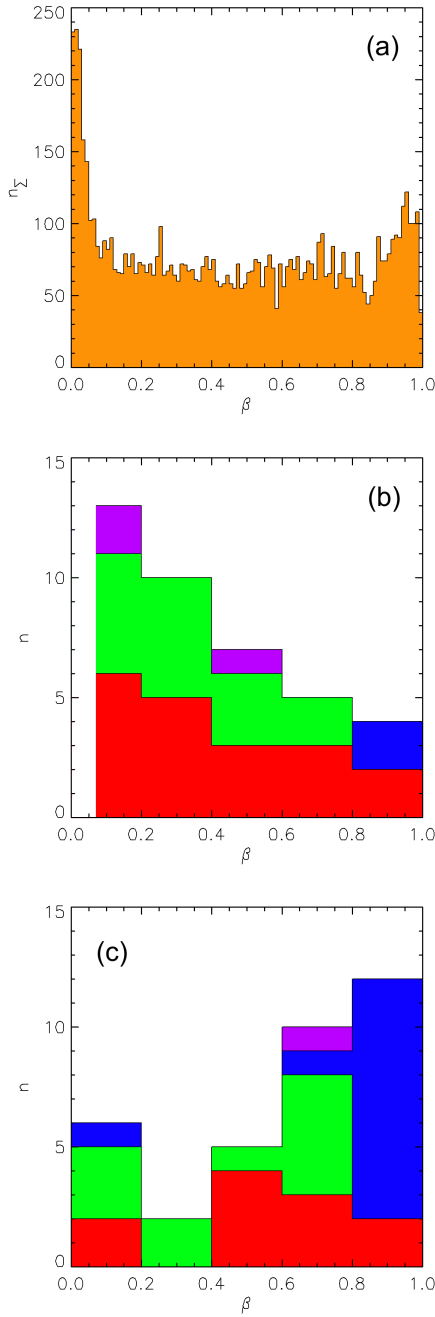


**Fig. 6.** Distributions of the impact parameter  $\beta$  estimates: *panel a*: over the whole list of KOIs in the NASA Exoplanet Archive. *Panel b*: for the KOIs from Table A.1 with  $\beta > 0.07$  and  $r_{se} < 0$ . *Panel c*: for the KOIs from Table A.1 with  $\beta > 0.07$  and  $r_{se} > 0$ . The ordinate value  $n$  is the number of  $\beta$ -estimates in a bin of histogram. Similarly to Fig. 3, color shows the status of objects within a bin: violet – probably non-planets (“n” in Table A.1); blue – candidates (“c” in Table A.1); green – confirmed planets, but with unknown masses (“p” in Table A.1); red – confirmed planets with measured planetary masses (“p!” in Table A.1). Cases with “\*” and “?” are also included.

at  $\beta \approx 1$ . The cases with  $r_{se} > 0$  correspond to the TLC shifting as a whole, which is known as the transit timing variability (TTV in Holczer et al. 2016). This effect, likely connected with the celestial-mechanic perturbations, complicates the analysis by adding a new term in Eq. (1). This complicated case is beyond the scope of our study. At the same time, the cases with negative correlation  $r_{se} < 0$ , corresponding to the negligible TTV, admit further simple diagnostics, which is demonstrated below.

We interpret the histogram maximum in Fig. 6b as a manifestation of increased  $\sigma_{s,e}$  related with the negative correlation  $r_{se}$ . The latter was a criterion for the inclusion of a case in the histogram. In particular, the histogram maximum (maximal value of  $n$ ) in Fig. 6b indicates the maximal  $\sigma_{s,e}$  at  $\beta \approx 0$ . This fact contradicts the hypothesis of a varying  $\beta$  and therefore indicates that the neglecting by the variations of  $R_p$ , done above, is an inconsistent assumption. Therefore, the effect of varying  $R_p$  (i.e., second term in Eq. (7)) dominates. Hence, the corresponding derivatives  $\partial\sigma_{s,e}/\partial\beta$  and  $\partial\sigma_{Rp}/\partial\beta$  are negative in Eq. (7). Moreover, the negative  $\partial\sigma_{s,e}/\partial\beta$  is directly seen in Fig. 7, prepared for the most reliable cases with the standard error of border timing estimates  $\varepsilon_{s,e} < 0.0007$  days, found in terms of the coefficient errors of the approximating polynomials and averaged over all time-windows. We note that only objects with  $r_{se} < 0$  and  $\beta > 0.07$  (like in Fig. 6b) were included in Fig. 7. In particular, Figs. 7c and d is constructed only for confirmed planets. The fact that Figs. 7a and b and Figs. 7c and d are almost the same suggests that the possible non-planetary objects have a negligible influence on the overall result.

The physical meaning of the shown gradients  $\partial\sigma_{s,e}/\partial\beta$  can be demonstrated using transformations  $\beta \rightarrow \gamma$  and  $\sigma_{s,e} \rightarrow \sigma_{Rp}$ , where  $\gamma$  is the positional angle as defined above (see Fig. 5) and  $\sigma_{Rp} = \sqrt{\langle(\Delta R_p)^2\rangle}$  is the standard deviation of the local radius of the planet at the start/end point of its ingress/egress on the stellar disk (i.e., point “c” in Fig. 5). The radius fluctuation  $\Delta R_p$  can be found from the triangle  $\Delta TMS$  with the side  $TM = x$  in Fig. 5. As  $x = \sqrt{(R_* + R_p)^2 - (\beta R_*)^2}$ , one can express  $R_p = \sqrt{x^2 + (\beta R_*)^2} - R_*$  and find its fluctuation, which corresponds to the fluctuation  $\Delta x$ , by differentiating  $\Delta R_p = (\partial R_p/\partial x)\Delta x = x\Delta x/\sqrt{x^2 + (\beta R_*)^2}$ . Assuming  $\Delta x \ll x$ , one can transform the fluctuations  $\Delta R_p$  and  $\Delta x$  into the standard deviations  $\sigma_{Rp} = \sqrt{\langle(\Delta R_p)^2\rangle}$  and  $\sigma_{s,e} = \sqrt{\langle(\Delta x)^2\rangle}/V_p$ , respectively. Taking into account the fact that the squared derivative can be expressed as  $(\partial R_p/\partial x)^2 = x^2/[x^2 + (\beta R_*)^2] = 1/[1 + (\tan \gamma)^2] = (\cos \gamma)^2$ , one can write  $\sigma_{Rp} = \sigma_{s,e} V_p \cos \gamma$ . To approximate the true value of the standard deviation of estimates of the transit borders’ timing, we introduce its corrected version  $\sigma_{s,e}^c = \sqrt{\sigma_{s,e}^2 - \varepsilon_{s,e}^2}$ , which takes into account the calculation error  $\varepsilon_{s,e}$  found as an error of the coefficient  $c_{s,e}$  in the approximating polynomials for the transit-borders in TLC (see Sect. 2.1), averaged over all time windows. Using the corrected value  $\sigma_{s,e}^c$  enables us minimize the artificial increase of  $\sigma_{Rp}$  during the grazing transits at large  $\beta$  and related positional angles  $\gamma$ . For the objects with  $\sigma_{s,e} < \varepsilon_{s,e}$ , the calculation of  $\sigma_{s,e}^c$  is impossible, and so zero values are adopted in such cases. As a result, one obtains the relative radius deviation  $\sigma_{Rp}/R_p$  of a variable transiting object:

$$\frac{\sigma_{Rp}}{R_p} = \frac{V_p \cos \gamma}{R_p} \sigma_{s,e}^c. \quad (8)$$

In Figure 8, which shows  $\sigma_{Rp}/R_p$  versus  $\gamma$  for the most reliable cases (i.e., confirmed planets with  $r_{se} < 0$ ,  $\beta > 0.07$ , and border timing errors  $\varepsilon_{s,e} < 0.0007$  days), one can see the clusters of increased  $\sigma_{Rp}/R_p$  values at low  $\gamma$ . Altogether, Figs. 6b, 7, and 8 show results that support the existence of variable obscuring zones (VOZ) around some KOIs at altitudes up to  $\sim 0.1 R_p$  near the orbital plane ( $\gamma \lesssim 50$  deg.). In this respect, it is worth noting that the parameter  $R_p$  used above should be understood in the sense of effective local radius of the transiter at the moment of its first (or last) contact with the stellar disk. The linear regressions

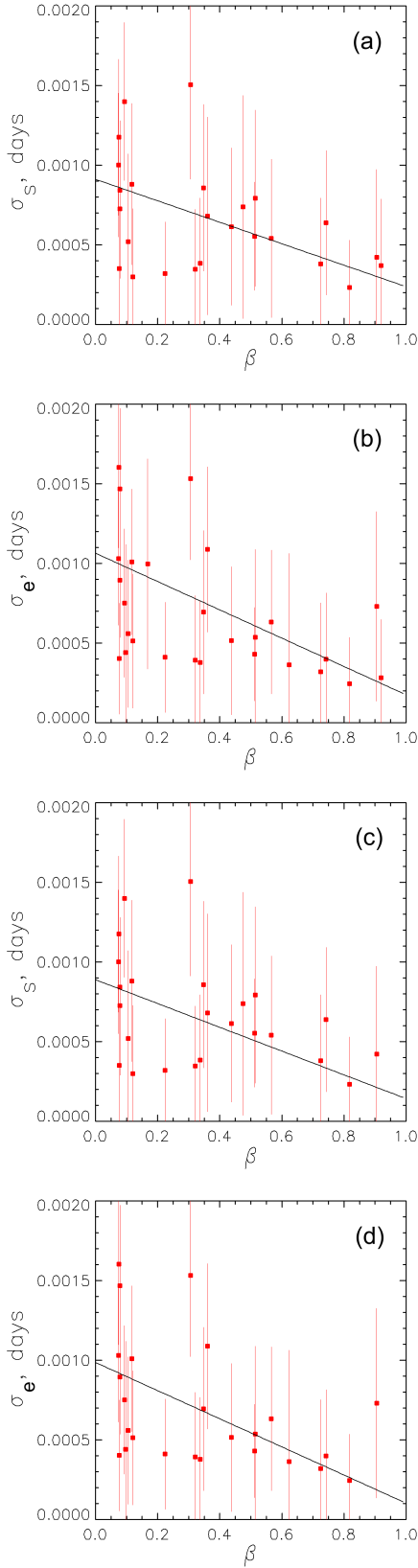


**Fig. 7.** Deviation,  $\sigma_{s,e}$ , of transit borders' timing, versus  $\beta$  estimates, confirming the negative derivative  $\partial\sigma_{s,e}/\partial\beta$  in Eq. (7) for the ingress (*panel a*) and egress (*panel b*) parts of the TLC. Only objects with  $r_{se} < 0$ ,  $\beta > 0.07$ , and border timing errors  $\varepsilon_{s,e} < 0.0007$  days from Table A.1 were included. The solid lines show the corresponding regressions. *Panels c* and *d* are the same as *panels a* and *b*, but for the confirmed planets with status “p” only, irrespective of extensions (“!”, “\*”, “?”).

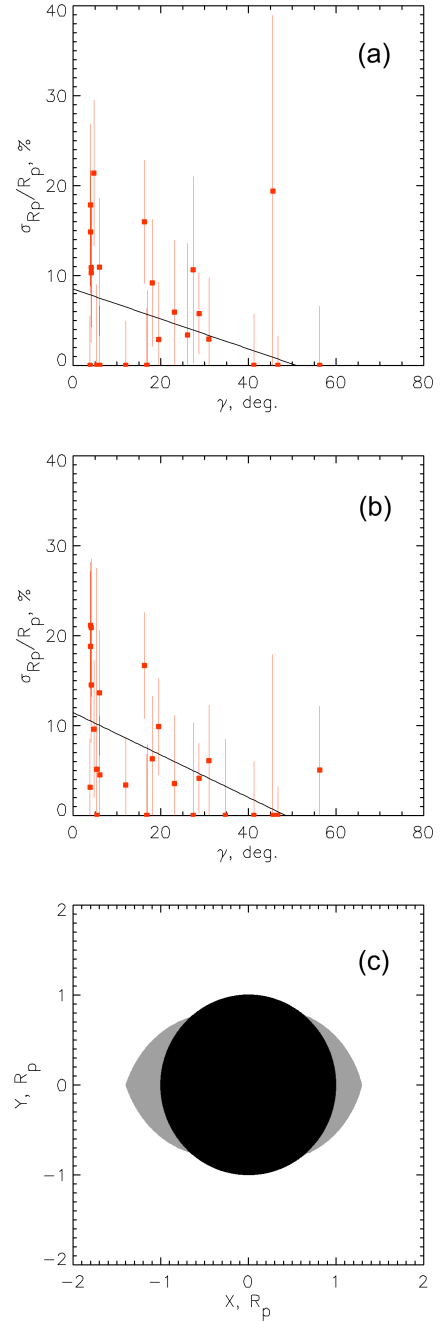


**Fig. 8.** Relative radius deviation  $\sigma_{Rp}/R_p$  vs. positional angle  $\gamma$  for the ingress (*panel a*) and egress (*panel b*) phases of confirmed planets. The range of effective radius variability of a KOI was calculated using Eq. (8) and the timing standard deviations from Figs. 7c and d. The lines show the corresponding regressions. Using these regressions, a generalized shape of the VOZ (gray color) around a KOI (black disk) is visualized in *panel c*.

$\langle\sigma_{Rp}/R_p\rangle = G\gamma + Q$ , were found with  $G = -0.17 \pm 0.08\%/deg$ ,  $Q = 8.51 \pm 2.24\%$  for the ingress and  $G = -0.24 \pm 0.08\%/deg$ ,  $Q = 11.46 \pm 2.17\%$  for the egress, respectively (see the lines in Fig. 8). Using these regressions one can estimate the borders of VOZ in the stellar disk in the corresponding Cartesian coordinates as follows:

$$\frac{X}{R_p} = \left( \sqrt{12} \left\langle \frac{\sigma_{Rp}}{R_p} \right\rangle + 1 \right) \cos \gamma, \quad (9)$$

$$\frac{Y}{R_p} = \pm \left( \sqrt{12} \left\langle \frac{\sigma_{Rp}}{R_p} \right\rangle + 1 \right) \sin \gamma, \quad (10)$$

where  $\sqrt{12}$  is the ratio of the amplitude of randomized  $\Delta R_p$  to its standard deviation, assuming a homogenous distribution function.

The  $X$  axis is directed along the visible KOI movement and is positive in the ingress and negative in the egress scenarios. Since photometry cannot distinguish between positive and negative values of  $\beta$ , or of  $\gamma$ , both options  $\pm Y$  naturally contribute to the recovered shape of VOZ (i.e., the range of KOI's effective radius fluctuation) shown in Fig. 8c. This shape confirms the conclusion on  $\partial\sigma_{Rp}/\partial\beta < 0$  in the above comparative analysis of histograms in Fig. 6. Hence, a typical KOI with  $r_{s,e} < 0$  shows signs of variable size along its orbital path (i.e., along the  $X$  axis).

Although Fig. 8 shows some asymmetry in the VOZ between its ingress and egress parts, this effect is not significant because the maximal difference between  $\left\langle \frac{\sigma_{Rp}}{R_p} \right\rangle = Q$  at  $\gamma = 0$  as well as the corresponding  $X/R_p$  (see Eq. (9)) for the ingress and egress are approximately equal to their standard errors. Figure 9a, constructed only for the confirmed planets, shows that in general  $\sigma_s \approx \sigma_e$ . However, the maximum of the histogram in Fig. 9b is shifted toward higher values of  $\sigma_s$  relative to the corresponding maximum in Fig. 9c. The histogram of difference  $\Delta\sigma \equiv \sigma_s - \sigma_e$  in Fig. 9d has the significantly positive skewness  $S = 1.81$  which is defined as

$$S = \frac{\sqrt{m(m-1)}}{m-2} \left\{ \frac{\frac{1}{m} \sum_{i=1}^m (\Delta\sigma_i - \langle \Delta\sigma \rangle)^3}{\left[ \frac{1}{m} \sum_{i=1}^m (\Delta\sigma_i - \langle \Delta\sigma \rangle)^2 \right]^{3/2}} \right\}, \quad (11)$$

where  $\Delta\sigma_i$  is an estimate of  $\Delta\sigma$  for an individual KOI with number  $i$ ;  $\langle \Delta\sigma \rangle$  is an averaged value over all  $\Delta\sigma_i$  estimates; and  $m = 73$  is the total number of considered objects. We note that non-planets and unconfirmed candidates are ignored here. For the normal distribution, the sample skewness has an expected zero value and a standard error  $\sigma_o = \sqrt{6m(m-1)/[(m-2)(m+1)(m+3)]} = 0.28$  (Kendall & Stuart 1969). The null hypothesis (i.e.,  $S = 0$ ) is rather unlikely, because in our case  $S/\sigma_o = 1.81/0.28 = 6.5$ . Hence, there is the slight statistical asymmetry  $\sigma_s > \sigma_e$ .

### 3.2. Transit shape analysis

Figure 10a shows the distribution of  $\langle A_s \rangle$  estimates for all KOIs from Table A.1. One can see that the histogram has a maximum at  $\langle A_s \rangle = 0.5$ , which is typical for a symmetric transiter. However, there is the significant skewness of this distribution:  $S = 3.63 \pm 0.24$  for all objects in the analyzed data set, and  $S = 3.48 \pm 0.28$  for the confirmed planets, i.e., objects marked with green and red in the figure. These values of  $S$  are  $15.1\sigma_0$  and  $12.4\sigma_0$  respectively, where  $\sigma_0 = 0.24$  and  $0.28$  are the corresponding standard errors for the normal distribution with  $S = 0$  (see details in Sect. 3.1). As the found skewness is significant and positive, there is an excess of transiting bodies with a slight TLC asymmetry  $A_s > 0.5$ , hence the increased radius of a shadow on its leading limb. Although this asymmetry is significant as a cumulative effect over both considered sets of objects (i.e., all KOIs from Table A.1 and those with the confirmed planet status), individual estimates of the transit shape parameter rarely show significant deviation of  $A_s$  from the value 0.5 of a symmetric TLC. Such deviated estimates are shown in Figure 10b.

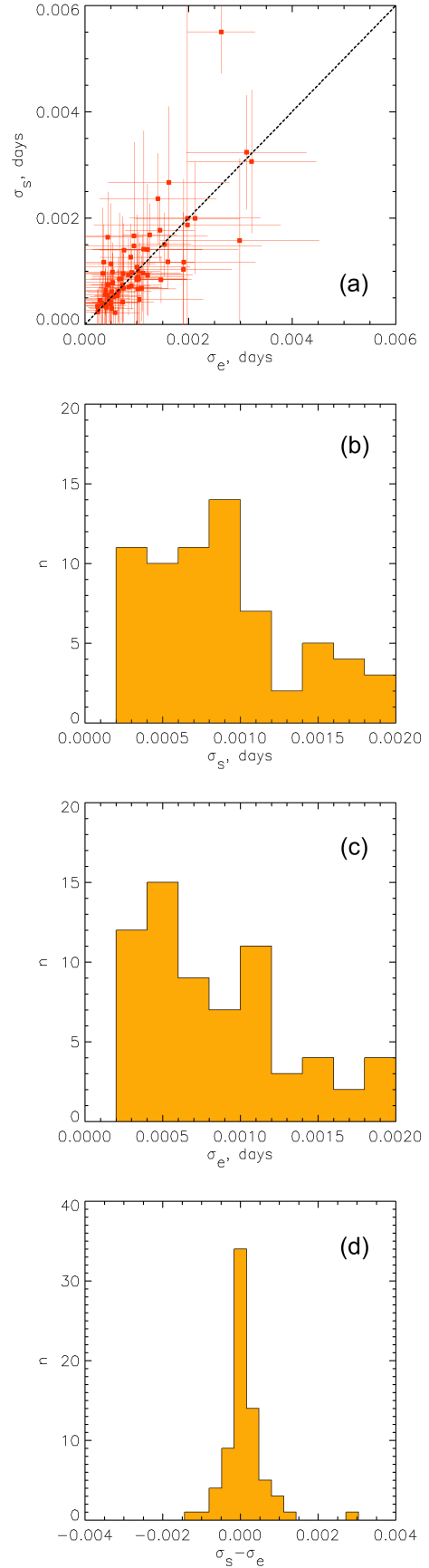


**Fig. 9.** Comparison of standard deviations of the transit border timing: *panel a:*  $\sigma_s$  vs.  $\sigma_e$ . *Panel b:* distribution histogram of  $\sigma_s$ . *Panel c:* distribution histogram of  $\sigma_e$ . *Panel d:* distribution histogram of  $\sigma_s - \sigma_e$ . Only confirmed planets from Table A.1 were considered.

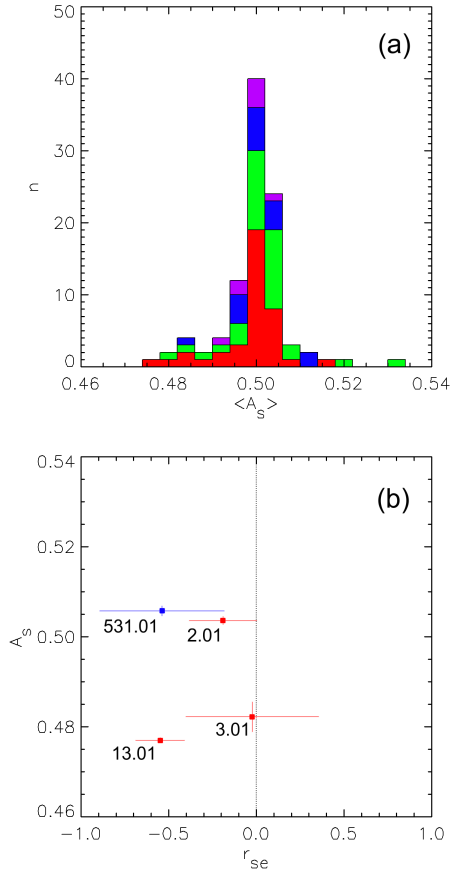


**Fig. 10.** Average TLC shape parameter  $\langle A_s \rangle$  for all KOIs from Table A.1: *panel a*: distribution histogram of  $\langle A_s \rangle$ . *Panel b*:  $\langle A_s \rangle$  versus  $r_{se}$  for significantly non-symmetric TLCs with  $|\langle A_s \rangle - 0.5| > 3\sigma_A$ . The KOI numbers are labeled (no non-stellar objects among them). The color coding of the KOI status is similar to one used in Figs. 3 and 6.

It is remarkable that the KOIs with significant TLC asymmetry  $|\langle A_s \rangle - 0.5| > 3\sigma_A$ , where  $\sigma_A$  is the standard deviation of  $A_s$  (given in Table A.1), are also associated with the negative cross-correlation  $r_{se}$ . We note that the distribution of the TLC shape parameter  $A_s$  for planets with measured masses (marked red in Fig. 10a) has the negative skewness  $S = -0.93 \pm 0.38$  related with the distribution tail at  $A_s < 0.5$ . This fact could be interpreted in terms of light-obscuring tail-like features of some planets. Such tailed bodies slightly affect overall statistics with positive  $S$ .

Figure 11 shows the histograms of the estimated Pearson correlation coefficients between the timing parameters  $\Delta t_s$ ,  $\Delta t_e$ , and  $\Delta t_m$  of TLCs and the transit shape parameter  $A_s$ . One can see that the transit asymmetry is controlled mainly by  $\Delta t_m$ , which is indicated by the maximum in the histogram in Fig. 11a at  $r_{Am} = 0.9 \pm 0.1$ , including 62% of cases. At the same time, the transit borders according to the maxima in histograms in Fig. 11b and c show lower correlations of  $r_{As} = -0.5 \pm 0.1$  and  $r_{Ae} = -0.5 \pm 0.1$ .

To interpret Fig. 11, one should consider the influence of small fluctuations of the transit timing  $\delta(\Delta t_s)$ ,  $\delta(\Delta t_m)$ , and  $\delta(\Delta t_e)$  on the variation of the transit shape parameter  $A_s = (\Delta t_m - \Delta t_s)/(\Delta t_e - \Delta t_s)$ :

$$\delta A_s \approx \frac{\partial(A_s)}{\partial(\Delta t_s)} \delta(\Delta t_s) + \frac{\partial(A_s)}{\partial(\Delta t_m)} \delta(\Delta t_m) + \frac{\partial(A_s)}{\partial(\Delta t_e)} \delta(\Delta t_e), \quad (12)$$

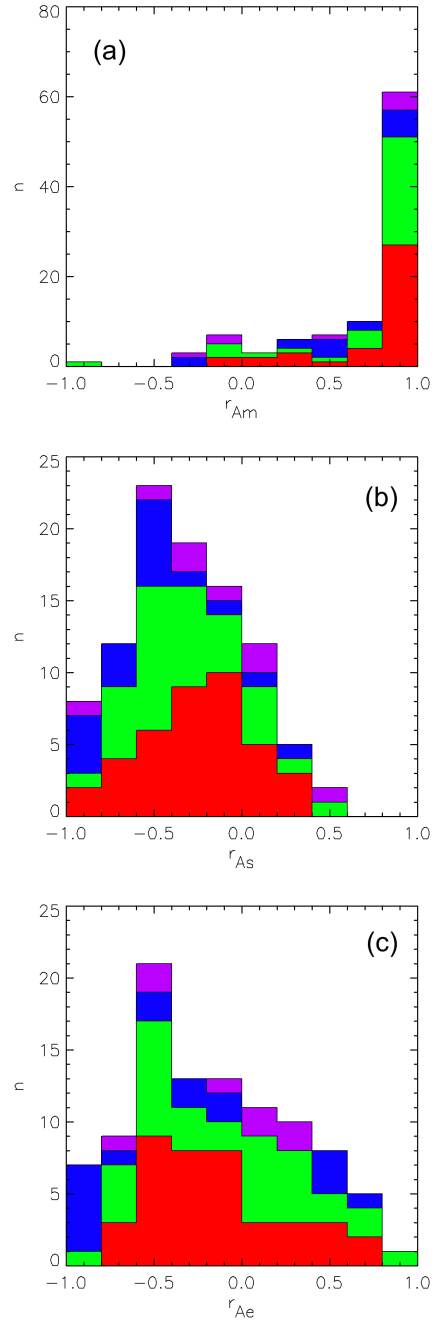


**Fig. 11.** Pearson correlation coefficients between the transit shape parameter  $A_s$  and TLC timing parameters: *panel a*: distribution histogram of  $r_{Am}$  – the correlation between  $A_s$  and  $\Delta t_m$ . *Panel b*: distribution histogram of  $r_{As}$  – the correlation between  $A_s$  and  $\Delta t_s$ . *Panel c*: distribution histogram of  $r_{Ae}$  – the correlation between  $A_s$  and  $\Delta t_e$ . Color shows the status of objects within a bin, as in Figs. 3 and 6.

where the partial derivatives of  $A_s$  are

$$\frac{\partial(A_s)}{\partial(\Delta t_s)} = -\frac{\Delta t_e - \Delta t_m}{(\Delta t_e - \Delta t_s)^2} \approx -\frac{1}{2D}, \quad (13)$$

$$\frac{\partial(A_s)}{\partial(\Delta t_m)} = \frac{\Delta t_e - \Delta t_s}{(\Delta t_e - \Delta t_s)^2} \approx \frac{1}{D}, \quad (14)$$

$$\frac{\partial(A_s)}{\partial(\Delta t_e)} = -\frac{\Delta t_m - \Delta t_s}{(\Delta t_e - \Delta t_s)^2} \approx -\frac{1}{2D}. \quad (15)$$

In Eqs. (13)–(15) we introduce the notation  $D \equiv \Delta t_e - \Delta t_s \approx \Delta t_{tr} + \delta t_L$  and express  $\Delta t_m - \Delta t_s \approx \Delta t_e - \Delta t_m \approx 0.5D$  assuming a quasi-symmetric TLC. Correspondingly, the correlation coefficients are

$$r_{As} = \frac{\langle \delta A_s \delta(\Delta t_s) \rangle}{\sigma_A \sigma_s} \approx -\frac{\sigma_s}{2D\sigma_A} + \frac{r_{ms}\sigma_m}{D\sigma_A} - \frac{r_{se}\sigma_e}{2D\sigma_A}, \quad (16)$$

$$r_{Am} = \frac{\langle \delta A_s \delta(\Delta t_m) \rangle}{\sigma_A \sigma_m} \approx -\frac{r_{ms}\sigma_s}{2D\sigma_A} + \frac{\sigma_m}{D\sigma_A} - \frac{r_{me}\sigma_e}{2D\sigma_A}, \quad (17)$$

$$r_{Ae} = \frac{\langle \delta A_s \delta(\Delta t_e) \rangle}{\sigma_A \sigma_e} \approx -\frac{r_{se}\sigma_s}{2D\sigma_A} + \frac{r_{me}\sigma_m}{D\sigma_A} - \frac{\sigma_e}{2D\sigma_A}, \quad (18)$$

where  $\sigma_A \equiv \sqrt{\langle \delta A_s^2 \rangle}$ ,  $\sigma_s$ ,  $\sigma_m$ , and  $\sigma_e$  are the standard deviations of  $A_s$ ,  $\Delta t_s$ ,  $\Delta t_m$ , and  $\Delta t_e$ , respectively.

Let us begin with a hypothesis that the timing changes are only due to statistical error without any connection some physical effect or process. In this case one might expect uncorrelated fluctuations of timing (i.e.,  $r_{se} = r_{ms} = r_{me} = 0$ ). Correspondingly, the shape-parameter fluctuation in Eq. (12) can be transformed into a standard deviation:

$$\sigma_A = \sqrt{\langle (\delta A_s)^2 \rangle} = \frac{1}{D} \sqrt{\frac{\sigma_s^2}{4} + \sigma_m^2 + \frac{\sigma_e^2}{4}}. \quad (19)$$

Substituting Eq. (19) into Eq. (17) with  $r_{ms} = r_{me} = 0$ , one obtains

$$r_{Am} = \frac{1}{\sqrt{1 + \left(\frac{\sigma_s}{2\sigma_m}\right)^2 + \left(\frac{\sigma_e}{2\sigma_m}\right)^2}}. \quad (20)$$

Equation (20) shows that  $r_{Am}$  is always positive ( $0 < r_{Am} < 1$ ). The most probable correlation  $r_{Am} > 0.8$  in Fig. 11a is possibly provided by the following condition:

$$\frac{\sqrt{\sigma_s^2 + \sigma_e^2}}{\sigma_m} < 2 \sqrt{\frac{1}{(0.8)^2} - 1} = 1.5. \quad (21)$$

As a quasi-flat minimum of TLC is harder to localize than the border timing, the realistic condition  $\sigma_{s,e} \lesssim \sigma_m$  is reasonable. However, an obviously unrealistic condition  $\sigma_{s,e} \gg \sigma_m$  is needed for  $r_{Am} \approx 0$ . Nevertheless, one can see that the histogram in Fig. 11a continues even further, in the region  $r_{Am} \lesssim 0$ , which contradicts Eq. (20).

Using Eqs. (16) and (19) for  $r_{ms} = r_{se} = 0$ , one can derive the expression for  $r_{As}$

$$r_{As} = -\frac{1}{\sqrt{1 + \left(2\frac{\sigma_m}{\sigma_s}\right)^2 + \left(\frac{\sigma_e}{\sigma_s}\right)^2}}. \quad (22)$$

Equation (22) shows that  $r_{As}$  is always negative. Nevertheless, the histogram in Fig. 11b has a continuation in the positive region of  $r_{As} > 0$ , which is true for 19% of the considered KOIs. The analogous continuation of the histogram of  $r_{Ae}$  in the region of positive values  $r_{Ae} > 0$  is even more prominent and takes place for 35% of cases in Fig. 11c, although Eq. (18) predicts negative  $r_{Ae}$  for  $r_{se} = r_{me} = 0$ ,

$$r_{Ae} = -\frac{1}{\sqrt{1 + \left(\frac{\sigma_s}{\sigma_e}\right)^2 + \left(2\frac{\sigma_m}{\sigma_e}\right)^2}}. \quad (23)$$

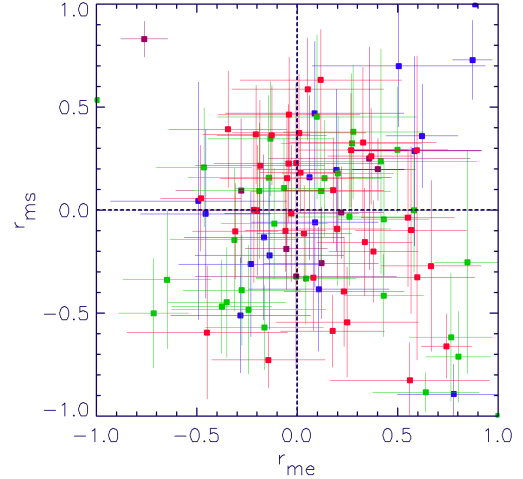


**Fig. 12.** Distribution of  $r_{ms}$  vs.  $r_{me}$  according Table A.1. Color shows the status of objects, as in Fig. 3.

Now, let us test the above assumption of  $r_{ms} = r_{me} = 0$  with the diagram  $r_{ms}$  versus  $r_{me}$ . In Fig. 12 one can see a clustering of most estimate points around  $r_{ms} = r_{me} = 0$  in accordance with the typical error bars. However, there are highly deviating points and even an outlying cluster at  $r_{ms} < -0.5$  and  $r_{me} > 0.5$ . This fact together with the values  $r_{As} > 0$  and  $r_{Ae} > 0$  forbidden for  $r_{ms} = r_{me} = 0$  leads us to suspect that the uncorrelated timing changes are not the only factor contributing to  $r_{ms}$  and  $r_{me}$ .

The most reasonable physical interpretation of the dominating influence of  $\Delta t_m$  on  $A_s$  is the strong effect of starspots which may slightly shift  $\Delta t_m$  in the central part of the TLC. However, this effect should be weakened towards the transit borders due to the decrease of the visible area of a spot near the stellar limb (projection effect). Correspondingly, one can expect  $r_{ms} \approx 0$  and  $r_{me} \approx 0$ . In the cases of a dominating influence of spots (i.e.,  $\sigma_m \gg \sigma_{s,e}$ , hence, statistically  $|\delta(\Delta t_m)| \gg |\delta(\Delta t_{s,e})|$ ), it follows from Eqs. (12) and (14) that  $\delta A_s \approx \delta(\Delta t_m)/D$ . In this case, the variance of  $A_s$  is  $\langle \delta A_s^2 \rangle = \langle \delta(\Delta t_m)^2 \rangle / D^2$ , and the standard deviation is  $\sigma_A = (\langle \delta A_s^2 \rangle)^{1/2} = \sigma_m / D$ . Substitution of the latter in Eq. (17) with  $r_{ms} = r_{me} = 0$  gives  $r_{Am} = 1$ , which agrees with the histogram in Fig. 11a. The cases with significantly non-zero  $r_{ms}$  and  $r_{me}$  in Fig. 12 are not a problem in cases with strong spot effect, i.e.,  $\sigma_{s,e} \ll \sigma_m$ , meaning that the terms containing  $r_{ms}$  and  $r_{me}$  in Eq. (17) are negligible. Hence, the prediction  $r_{Am} \approx 1$  is still valid for any values of  $r_{ms}$  and  $r_{me}$  in the approximation of a strong spot effect.

For a moderate spot effect ( $\sigma_m \sim \sigma_{s,e}$ ), the first and third terms in Eq. (17) could give significantly negative deposits in  $r_{Am}$  when  $r_{ms} > 0$  and  $r_{me} > 0$ , respectively. Such an effect is possible in the case of TTVs (Holczer et al. 2016). When the TTV effect shifts the TLC as a whole, the positive correlations  $r_{ms} > 0$  and  $r_{me} > 0$  take place. The corresponding decrease of  $r_{Am}$  could explain the fact that many objects (38%) in Fig. 11a show a lower correlation  $r_{Am} < 0.8$  (up to negative values).

The positive correlations  $r_{As}$  and  $r_{Ae}$ , forbidden for the uncorrelated border timing fluctuations, may still take place due to statistical errors in the correlation coefficient estimates. The scale of the leakage of these estimates into regions  $r_{As} > 0$  and  $r_{Ae} > 0$  is of the same order as the statistical errors  $\sigma_{r_{As,e}} = (1 - r_{As,e}^2) / \sqrt{N_w - 1}$  of Pearson coefficients  $r_{As}$  or  $r_{Ae}$  for the correlations between the TLC shape parameter  $A_s$  and the border timing  $\Delta t_s$  or  $\Delta t_e$ . As the number  $N_w$  of the used time-windows

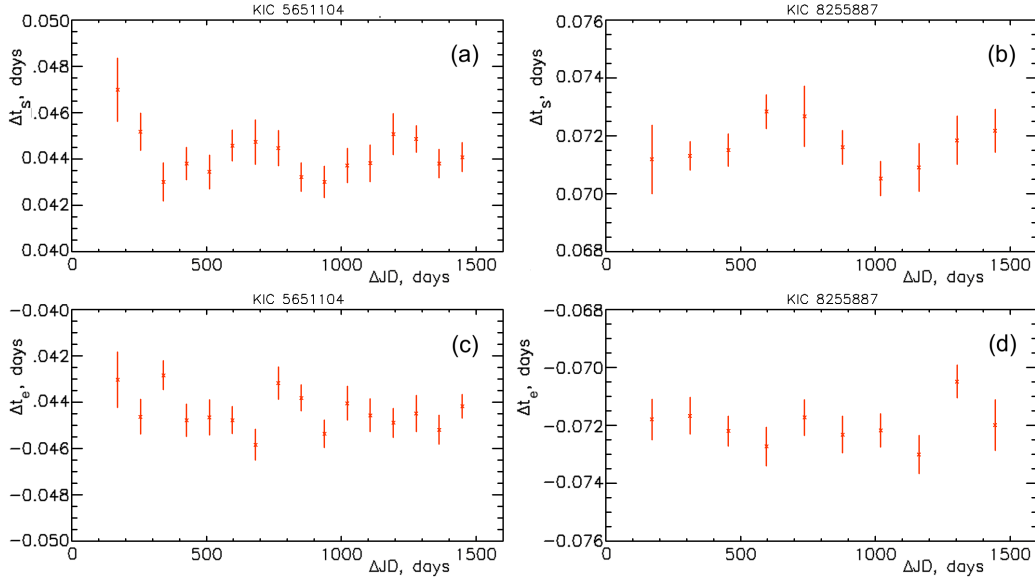


**Fig. 13.** Quasi-sinusoidal oscillations of  $\Delta t_s$  in TLCs of KOI 840.01 at KIC 5651104 (*panel a*) and KOI 908.01 at KIC 8255887 (*panel b*). For comparison, *panels c* and *d* show the chaotic behavior of  $\Delta t_e$  by the same objects.

is the same for  $r_{As}$  and  $r_{Ae}$  for each particular KOI, and the histograms of Figs. 11b,c are similar for negative correlations, one can predict the statistical proximity  $\sigma_{r_{As}} \approx \sigma_{r_{Ae}}$  and the similarity between these histograms in the regions of positive correlations  $r_{As} > 0$  and  $r_{Ae} > 0$ . Nevertheless, there is a noticeable asymmetry. Specifically, in the histogram of  $r_{Ae}$  (Fig. 11c), 35% of the considered objects have  $r_{Ae} > 0$ , while in the histogram of  $r_{As}$  (Fig. 11b) only 19% of the objects show a positive correlation  $r_{As} > 0$ . Therefore, there should be an additional source of positive correlation besides statistical errors.

The uncorrelated estimates of  $\Delta t_{s,m,e}$  as well as the spot effect justify the guess that  $r_{ms} = r_{me} = 0$ , making negligible the related terms in Eqs. (16) and (18), which could lead to positive deposits in  $r_{As}$  and  $r_{Ae}$ . Another source of the positive correlations  $r_{As} > 0$  and  $r_{Ae} > 0$  are the terms containing  $r_{se}$  in the same equations. If  $r_{se} < 0$ , as was demonstrated in Sect. 3.1, the third term in Eq. (16) and the first term in Eq. (18) give the positive deposits in  $r_{As}$  and  $r_{Ae}$ , respectively. The more pronounced (35% of cases) continuation of the histogram to the region  $r_{Ae} > 0$  in Fig. 11c, as compared with 19% of cases with  $r_{As} > 0$  in Fig. 11b, means that there is a statistical inequality  $\sigma_s > \sigma_e$  in the symmetric terms  $-r_{se}\sigma_s/(2D\sigma_A)$  and  $-r_{se}\sigma_e/(2D\sigma_A)$ . This results in the unequal positive deposits in  $r_{Ae}$  (see Eq. (18)) and in  $r_{As}$  (see Eq. (16)), which is consistent with the conclusions in Sect. 3.1 on detected statistical inequalities  $\sigma_s > \sigma_e$  and  $r_{se} < 0$  in many cases.

### 3.3. Individual peculiarities

In the case of non-varying transits, the estimates of timing parameters  $\Delta t_s$ ,  $\Delta t_e$ , and  $\Delta t_m$  are dispersed irregularly within the range of about plus or minus one standard error (Figs. 2a, b, and d). However, TLCs of KOI 840.01 and KOI 908.01, orbiting KIC 5651104 and KIC 8255887, respectively, show quasi-sinusoidal oscillations of  $\Delta t_s$  (Figs. 13a and b), whereas the behavior of  $\Delta t_e$  appears chaotic (Figs. 13c and d). Correspondingly, the cross-correlation  $r_{se}$  in Table A.1 is insignificant:  $0.37 \pm 0.31$  (for KOI 840.01) and  $0.37 \pm 0.31$  (for KOI 908.01).

Moreover, in some cases (see Fig. 14) there is a clear transit shape asymmetry (i.e.,  $A_s \neq 0.5$ ), which can also vary. The

known case of KOI 13.01 (KIC 9941662) in Fig. 14a has been interpreted as an example of gravity darkening effect appearing during a tilted transit in front of a fast rotating (the period is 1.06 days) star (Szabó et al. 2012 and therein). At the same time, it is worth mentioning that besides the typical gravity darkening phenomenology, the object KOI 13.01 also demonstrates a well-pronounced anti-correlation  $r_{se} = -0.55 \pm 0.14$  at the level beyond three standard errors ( $r_{se}/\varepsilon_{se} = 3.93$ , see in Table A.2). This attribute constitutes an additional enigma, which cannot be interpreted as merely a darkening effect and therefore suggests an additional manifestation of VOZ. Moreover, gravitational darkening is not valid at all in the case of KOI 3.01 (at KIC 10748390) in Fig. 14b, because its host star is a slow rotator with a period of  $\approx 30$  days (see Fig. 15).

Figure 16 shows clear cyclic variation of the visible transit duration  $D = \Delta t_e - \Delta t_s$ , as well as anti-correlation  $r_{se} = -0.57 \pm 0.11$  between  $\Delta t_s$  and  $\Delta t_e$  for the KOI 971.01 orbiting KIC 11180361. This system exhibits grazing transits, where less than half of the transiting shadow is projected onto the stellar disk. Such geometry, in combination with an extremely short transit period of  $P_{tr} = 0.533$  days, is very sensitive to variations in the size of the transiter. Based on the geometry treatment in Sect. 3.1, it can be shown that

$$\frac{1}{D} \frac{\partial D}{\partial z} = \frac{1+z}{(1+z)^2 - \beta^2} = 13.0, \quad (24)$$

where the planetary-to-stellar radius ratio  $z = R_p/R_* = 0.302$  and the impact parameter  $\beta = 1.263$  are defined with the cumulative data from NASA EA. Therefore, in order to provide the measured  $\pm 11\%$  of the relative variations of  $D$  (as seen in Fig. 16a), the ratio  $R_p/R_*$  according to Eq. (24) has to change within the range of  $\sim \pm 11\%/13 = \pm 0.8\%$ . We note that the star KIC 11180361 shows  $\delta$  Sct-type pulsations (Balona 2016), the period of which is nevertheless too short ( $\sim 0.1$  day) to be related with the cycles in Fig. 16a of  $\sim 500$  days. Although this system was considered as an eclipsing star (Slawson et al. 2011), no variations of radial velocity were detected, nor were signs of spectral contamination from the companion (Lampens et al. 2018). The current status of the KIC 11180361/KOI 971.01 in NASA EA is a candidate. Even if KIC 11180361/KOI 971.01 is a star, in light of

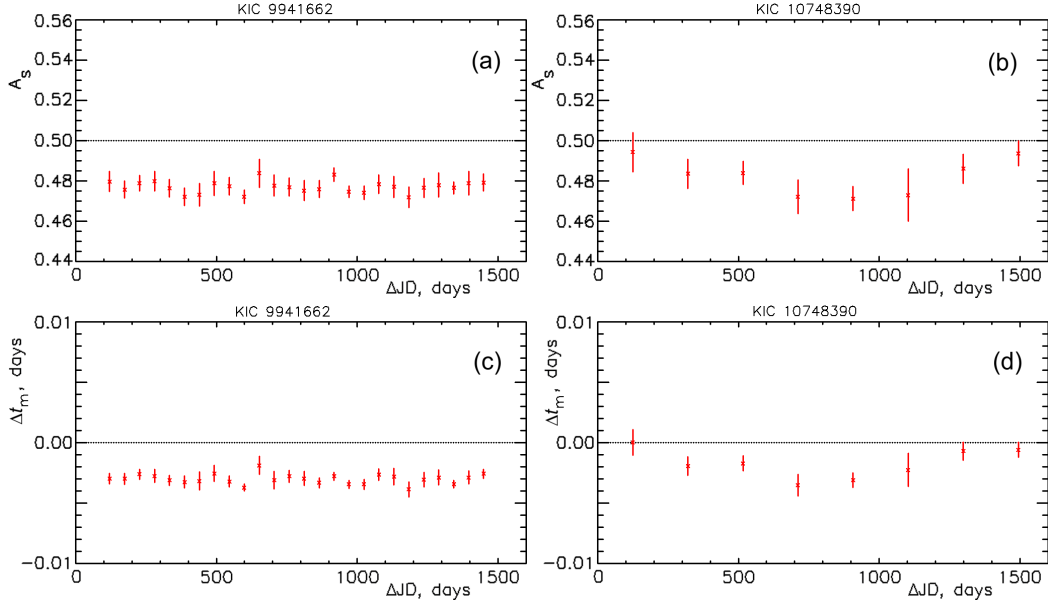


**Fig. 14.** Transit shape parameter  $A_s$  of KOI 13.01 orbiting KIC 9941662 (*panel a*) and KOI 3.01 at KIC 10748390 (*panel b*). For comparison, *panels c* and *d* show the synchronous variations of  $\Delta t_m$  by the same objects.

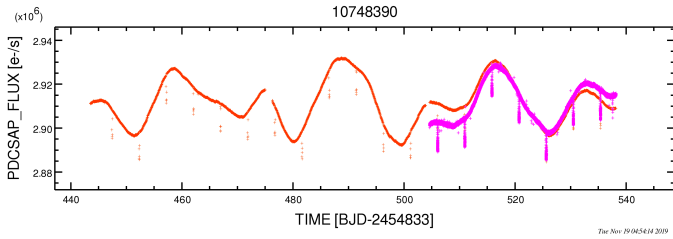


**Fig. 15.** Rotational modulation with a 30 day period in the light curve of KOI 3.01 hosted by KIC 10748390. The long- and short-cadence data are marked by the red and crimson colors, respectively.

its rather unique features, this object deserves a dedicated study, which we attempt to initiate here.

#### 4. Discussion

The host stars of all the KOIs considered here with varying transit border timings (Table A.2) are main sequence objects. This can be seen in an analog of the HR-diagram in Fig. 17 prepared for these objects, i.e., the logarithm of gravity  $\log(g)$  versus effective temperature  $T_{\text{eff}}$  in the stellar photospheres. A cluster of stars around the solar position can be clearly seen there. For example, KIC 12019440 has almost the same parameters as the Sun. The numerous attempts (Qu et al. 2015 and therein) to detect variability in the solar radius on long timescales from 1 day to decades give a negligible upper limit of the effect at the level of  $<0.5$  arcseconds or  $<0.05\%$ . At the same time, according to the analysis in Sect. 3.1, the distance  $\text{TS} = R_p + R_*$  in Fig. 5, which defines the transit border timing variations, changes much more than just only the varying stellar radius might contribute. In particular, the regressions in Figs. 8a and b reveal the variations of  $R_p$  with the scale of  $\sigma_{R_p}/R_p \approx 10\%$ , which yields an estimate of  $\sigma_{R_p}/R_* = (\sigma_{R_p}/R_p)(R_p/R_*) \sim 1\%$  for a typical hot jupiter ratio  $R_p/R_* \sim 0.1$ . We note that the sun-like stars show variability in their radii with an order of magnitude smaller amplitude than the observed scale of variations of  $\text{TS} = R_p + R_*$ . Therefore, the main

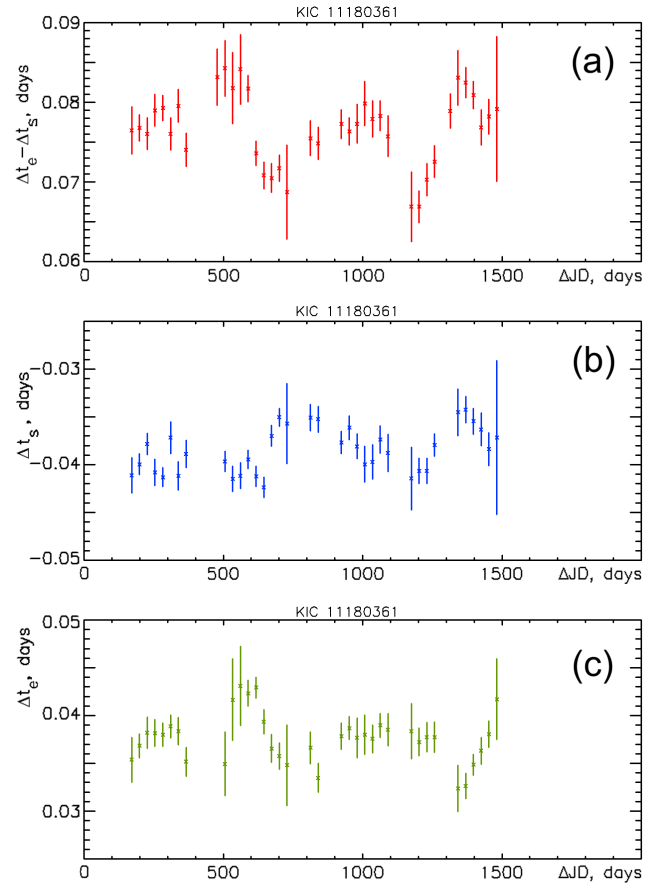


**Fig. 16.** Temporal variation of *panel a*: transit duration  $\Delta t_e - \Delta t_s$ ; *panel b*: transit start-time  $\Delta t_s$ , and *panel c*: transit end-time  $\Delta t_e$  in the extreme case of grazing transits of KOI 971.01 orbiting KIC 11180361.

source of TS variability is connected with the varying  $R_p$  rather than with  $R_s$ . This conclusion supports the constant  $R_s$  assumption, which is applied above during the derivation and analysis of Eqs. (1)–(10).

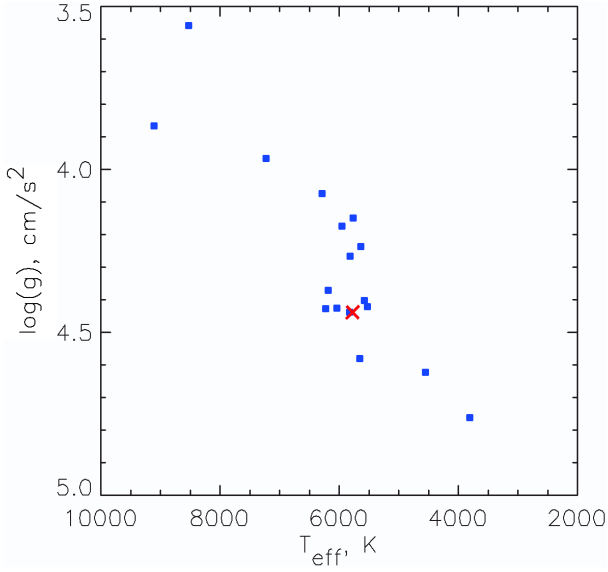


**Fig. 17.** Stellar gravity ( $\log(g)$ ) vs. effective temperature ( $T_{\text{eff}}$ ) distribution of the systems with the noticeably varying transit borders (see Table A.2) according to the NASA EA. The red cross marks the position of the Sun.

Let us verify whether or not the cyclic variability of  $\Delta t_s$ ,  $\Delta t_e$ , and  $\Delta t_m$  found above and the corresponding  $A_s$  could indicate the presence of precessing exo-rings or disks. To model these cyclic phenomena, we consider a transiting spherical planet orbiting a real star KIC 11359879 (host of Kepler-15b) with a planetocentric opaque disk tilted at 30 degrees relative the orbital plane and precessing with a period of 2400 days (see in Fig. 18a). For the reconstruction of the corresponding TLSs, we use a pixel-by-pixel integration, which can be used for any type or geometry of transiter. The dimming of stellar flux during the transit is characterized by the part of starlight blocked by the transiting object

$$\Delta F = \frac{\int \int I(x, y) dx dy}{\int \int I_s(x, y) dx dy}, \quad (25)$$

where we use a coordinate system co-centered on the stellar disk, with the  $x$ -axis along the planet orbit projection onto the stellar disk. By this,  $I_s$  is radiation intensity at a given position  $(x, y)$  on the visible stellar disk, and  $I$  is the same intensity but disturbed by the transiter. The integrals in Eq. (25) can be replaced by sums over  $N_p$  pixels with serial number  $i$ :

$$\Delta F = \frac{\sum_{i=1}^{N_p} I(x_i, y_i)}{\sum_{i=1}^{N_p} I_s(x_i, y_i)}. \quad (26)$$

The stellar limb darkening is taken into account according to the best (four coefficients) approximation by Claret & Bloemen (2011), depending on the particular stellar effective temperature and gravity adopted from NASA EA. The planetary data (radius  $R_p$ , semi-major axis  $a_p$  of the orbit, impact parameter  $\beta$ , mid-time  $t_0$  of the first observed transit, and transit period  $P_{\text{tr}}$ ) are also taken from the NASA Exoplanet Archive. In the reference system used here, the moving center of the exoplanetary shadow has coordinates

$$x_p = a_p \sin \left[ \frac{2\pi}{P_{\text{tr}}} (t - t_0) \right], \quad (27)$$

$$y_p = \beta R_*, \quad (28)$$

with the value for stellar radius  $R_*$  taken from NASA EA. Using this approach, we calculate a synthetic light curve, which is processed analogously to the real photometric data. Figure 18 summarizes the obtained results.

In particular, Fig. 18 reveals a clear variability in  $A_s$ ,  $\Delta t_s$ , and  $\Delta t_e$ , but an almost complete lack of noticeable variability in  $\Delta t_m$ . These results, to a certain degree, resemble the measured behavior of the TLC border timing and shape parameters of real objects shown in Figs. 13 and 14b and confirm that although the disk effectively influences the transit borders, it cannot noticeably displace  $\Delta t_m$  because of the transiter's symmetry. However, as shown in the analysis in Sect. 3.2, the varying minimum time  $\Delta t_m$  of the TLC is the main driver of the variations of its shape parameter  $A_s$ . This, in particular, results in the cross-correlation  $r_{\text{Am}}$  values close to unity obtained for the real objects with oscillating  $\Delta t_s$ , for example,  $r_{\text{Am}} = 0.98 \pm 0.02$  and  $0.94 \pm 0.05$  for KIC 8255887 and KIC 10748390 respectively. Altogether, this discrepancy, with regard to the relation between  $\Delta t_m$  and  $A_s$  as predicted by the model and revealed from observations, rules out the hypothesis of a precessing circumplanetary disk as the main driver of the varying TLC shape parameter, whereas the variation of only border timing in some cases could still be connected with such a disk.

As the TTV effect cannot influence the shape parameter  $A_s$ , as explained in Sect. 3.2, the measured (in some cases) phenomenon of a variable  $A_s$  remains to be related with the effect of starspots. If this is the case, then the regular variability of  $\Delta t_m$  and correspondingly  $A_s$  seen in Figs. 14b and d suggests some long-living ( $\sim 10^3$  days) starspot or activity complex in the stellar disk of KIC 10748390, the position of which appears to have a certain relation to the transiting exoplanet KOI 3.01. In other words, in order to have a quasi-stable, that is, detectable  $\Delta t_m \neq 0$  within one time-window, which at the same time can vary slightly from one time-window to another, the starspot(s) must occupy approximately the same position on the stellar disk during different transits in the window. Since in the considered case of KIC 10748390 the stellar rotation period is much longer ( $\approx 30$  days according to Fig. 15) than the transiter's orbital period ( $P_{\text{tr}} = 1.24$  days), the above-mentioned condition could be fulfilled if the starspot appearance is related with the planet. This conclusion does not seem impossible in light of recent reports on planetary related activity regions in host stars (e.g., Cauley et al. 2019 and therein). An alternative scenario with a transit over a polar starspot requires fast stellar rotation (Yadav et al. 2015) which is not the case in the stellar system considered here.

## 5. Conclusions

The results reported in this paper lead to several conclusions which can be summarized as follows.

1. The transit border timings of some KOIs (exclusively hot jupiters in Table A.2) are variable on timescales from  $\approx 400$  to  $\leq 1500$  days (see Figs. 4, 13 and 16).

2. Among the most typical features of the TLC timing variability is the significant anti-correlation  $r_{\text{se}} < 0$  between the transit border timing parameters  $\Delta t_s$  and  $\Delta t_e$  (see Table A.2 as well as Figs. 4, 16). This anti-correlation is likely a manifestation of the variability of the dimensions of KOIs. A hypothetical variability of the impact parameter or the stellar radius, assumed as an alternative mechanism for the anti-correlated TLC border timings were shown to contradict the revealed facts (see the argumentation in Sects. 3.1 and 4).

3. The range of variability in the dimensions of KOIs, introduced as a so-called varying obscuring zone (VOZ), extends

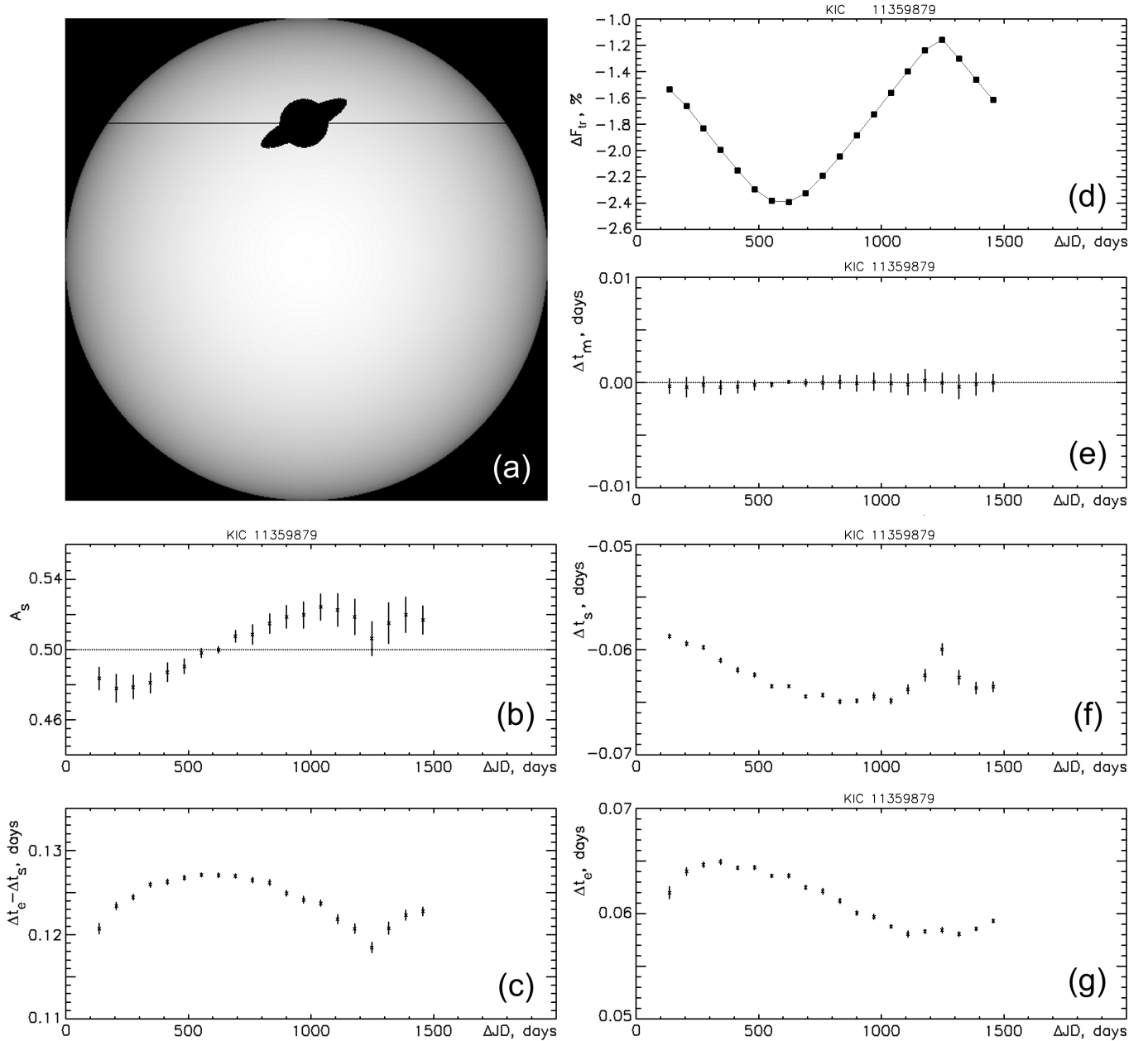


**Fig. 18.** Modeling of TLC variability for an analogue of Kepler-15b with a prescribed precessing ring: *panel a*: model image of the transiting exoplanet with a precessing ring (solid line shows the trajectory of planet). *Panel b*: variations of the shape parameter  $A_s$  of the simulated synthetic TLC. *Panel c*: variations of the simulated transit duration  $\Delta t_e - \Delta t_s$ . *Panel d*: variations of the simulated transit depth  $\Delta F_{tr}$ . *Panel e*: variations of the simulated TLC minimum time  $\Delta t_m$ . *Panel f*: variations of the simulated transit start-time  $\Delta t_s$ . *Panel g*: variations of the simulated transit end-time  $\Delta t_e$ . The abscissa scale  $\Delta\text{JD} = \text{JD} - 2\,454\,833.0$  is in Julian days (JD).

mainly along the orbit, up to a maximum of  $\sim 10\%$  of the transiter's size on average, and disappears in the perpendicular direction as shown in Fig. 8. This feature suggests generation of dust or aerosol in the upper layers of the atmospheres of KOIs and above, especially in the equatorial regions (i.e., close to the orbital plane), which are the subject of higher stellar radiative impact as compared to the poles.

4. The aerosol or dust particle clouds in the VOZ, detected in the present study, may also be connected with the detected dusty obscuring matter (DOM) ahead of hot jupiters at altitudes  $\sim 2R_p$  (Arkhyov et al. 2019). This assumption is in particular supported by the fact that the signatures of pre-transit DOM are detected for six KOIs (in Table 1 in Arkhyov et al. 2019)

that also have the varying transit borders timing (i.e., appear in Table A.2). These objects are the confirmed exoplanets KOI 13.01, KOI 17.01, KOI 18.01, KOI 20.01, and KOI 186.01, and the candidate exoplanet KOI 6085.01 (according to NASA EA). Indeed, as seen in the histograms in Figs. 10a and 9, there is a perceptible statistical excess of the ahead radius of the KOIs, estimated from the ingress part of the TLC, as compared to the opposite side values, which manifests itself as a significant positive skewness of the distribution of estimates for  $A_s$  and statistic inequality  $\sigma_s > \sigma_e$  (see Sect. 3).

5. Starspots appear to be the main factor disturbing the generally symmetric TLC shape (i.e., giving  $A_s \neq 0.5$ ). At the same time, the starspots usually have a limited lifetime and a

quasi-accidental (random) appearance in longitude. Thus, they should result in a disordered, irregular variability of  $A_s$ . Nevertheless, the system KIC 10748390 / KOI 3.01 demonstrates the regular variation of  $A_s$  on a timescale of  $\sim 10^3$  days (Fig. 14). This object is a candidate for having a starspot, which is associated (synchronized) with the transiter.

6. Altogether, the independent measurement of the transit border timing performed here opens a way to study yet unexplored phenomena, such as for example the oscillations in  $\Delta t_s$  (see Fig. 13).

In summary, we conclude that the transit border timing is a new and effective but still underused instrument for the in-transit probing of exoplanetary exteriors.

*Acknowledgements.* The authors acknowledge the projects I2939-N27 and S11606-N16 of the Austrian Science Fund (FWF) for the support. M.L.K. is grateful also to the grant No. 18-12-00080 of the Russian Science Foundation and acknowledges the project “Study of stars with exoplanets” within the grant No.075-15-2019-1875 from the government of Russian Federation.

## References

- Aizawa, M., Masuda, K., Kawahara, H., & Suto, Y. 2018, *AJ*, **155**, 206
- Almenara, J. M., Damiani, C., Bouchy, F., et al. 2015, *A&A*, **575**, A71
- Arkhypov, O. V., Khodachenko, M. L., & Hanslmeier, A., 2019, *A&A*, **631**, A152
- Balona, L. A. 2016, *MNRAS*, **459**, 1097
- Cauley, P. W., Shkolnik, E. L., Llama, J., & Lanza, A. F. 2019, *Nat. Astron.*, **3**, 1128
- Claret, A., & Bloemen, S. 2011, *A&A*, **529**, A75
- Esteves, L. J., De Mooij, E. J. W., & Jayawardhana, R. 2013, *ApJ*, **772**, 51
- Garai, Z. 2018, *A&A*, **611**, A63
- Holczer, T., Mazeh, T., Nachmani, G., et al. 2016, *ApJS*, **225**, 9
- Hotelling, H. 1953, *J. R. Stat. Soc. Ser B*, **15**, 193
- Jackson, B., Adams, E., Sandidge, W., Kreyche, S., & Briggs, J. 2019, *AJ*, **157**, 239
- Jenkins, J. M., Douglas, A.C., Chandrasekaran, H., et al. 2010, *ApJ*, **713**, L87
- Kendall, M. G., & Stuart, A. 1969, *The Advanced Theory of Statistics* (Houston: Griffin), 1
- Kepler Mission Team 2009, VizieR On-line Data Catalog: [V/133](#)
- Khodachenko, M. L., Shaikhislamov, I. F., Lammer, H., & Prokopov, P. A. 2015, *ApJ*, **813**, 50
- Lampens, P., Frémat, Y., Vermeylen, L., et al. 2018, *A&A*, **610**, A17
- Llama, J., Vidotto, A. A., Jardine, M., et al. 2013, *MNRAS*, **436**, 2179
- Morton, T. D., Bryson, S. T., Coughlin, et al. 2016, *ApJ*, **822**, 86
- Pass, E. K., Cowan, N. B., Cubillos, P. E., & Sklar, J. G. 2019, *MNRAS*, **489**, 941
- Qu, Z. N., Kong, D. F., Xiang, N. B., & Feng, W. 2015, *ApJ*, **798**, 113
- Rappaport, S., Gary, B. L., Kaye, T., et al. 2016, *MNRAS*, **458**, 3904
- Sanchis-Ojeda, R., Rappaport, S., Pallè, E., et al. 2015, *ApJ*, **812**, 112
- Schlichting, H. E., & Chang, Ph. 2011, *ApJ*, **734**, 117
- Slawson, R. W., Prsa, A., Welsh, W. F., et al. 2011, *AJ*, **142**, 160
- Szabó, G. M., Pál, A., Derekas, A., et al. 2012, *MNRAS*, **421**, L122
- Ulmer-Moll, S., Santos, N. C., Figueira, P., Brinchmann, J., & Faria, J. P. 2019, *A&A*, **630**, A135
- Wang, L., & Dai, F. 2019, *ApJ*, **873**, L1
- Yadav, R. K., Gastine, T., Christensen, U. R., & Reiners, A. 2015, *A&A*, **573**, A68

## Appendix A: Tables

Table A.1. Analyzed target set and main processing results.

KIC <sup>(a)</sup>	KOI <sup>(b)</sup>	Sta- tus <sup>(d)</sup>	$\sigma_m$ 10 <sup>-3</sup> days	$\sigma_s$ 10 <sup>-3</sup> days	$\sigma_e$ 10 <sup>-3</sup> days	$r_{ms}$	$r_{me}$	$r_{se}$	$\langle A_s \rangle$ <sup>(c)</sup>
757450	889.01	p!	0.79	0.93	1.21	0.33 ± 0.36	0.33 ± 0.36	0.01 ± 0.41	0.500 ± 0.003
7585481	890.01	p	7.26	0.85	1.00	-0.34 ± 0.33	-0.65 ± 0.22	-0.15 ± 0.37	0.504 ± 0.015
2571238	84.01	p!	4.72	1.58	2.99	-0.27 ± 0.41	0.67 ± 0.25	0.38 ± 0.38	0.490 ± 0.012
2987027	197.01	p	2.45	1.77	1.44	0.16 ± 0.40	-0.14 ± 0.40	0.80 ± 0.15	0.506 ± 0.006
3351888	801.01	p	1.93	0.62	0.65	0.11 ± 0.24	-0.07 ± 0.24	0.34 ± 0.21	0.506 ± 0.004
3544595	69.01	p!	4.32	0.47	1.05	0.22 ± 0.32	-0.18 ± 0.32	0.47 ± 0.26	0.492 ± 0.010
3749365	1176.01	p	0.48	0.38	0.38	0.18 ± 0.28	0.20 ± 0.28	-0.61 ± 0.18	0.497 ± 0.001
3762468	208.01	p	4.15	5.50	2.63	0.32 ± 0.34	0.27 ± 0.35	0.19 ± 0.36	0.505 ± 0.010
3861595	4.01	p!?	2.19	0.85	0.66	-0.02 ± 0.33	-0.03 ± 0.33	0.50 ± 0.25	0.508 ± 0.006
3935914	809.01	p	0.91	0.79	0.54	-0.33 ± 0.22	0.04 ± 0.25	-0.24 ± 0.24	0.504 ± 0.003
4055765	100.01	c	1.26	1.21	1.95	0.20 ± 0.39	0.19 ± 0.39	0.46 ± 0.32	0.503 ± 0.003
4178389	185.01	c?	0.22	0.65	0.66	0.70 ± 0.30	0.51 ± 0.43	0.51 ± 0.43	0.500 ± 0.002
4180280	144.01	p	6.69	1.48	0.95	0.21 ± 0.29	-0.46 ± 0.24	0.27 ± 0.28	0.480 ± 0.012
4570949	1658.01	p!*	0.10	0.49	0.47	-0.33 ± 0.26	0.08 ± 0.29	0.03 ± 0.29	0.500 ± 0.001
4742414	631.01	n	5.94	1.00	1.53	0.09 ± 0.35	-0.28 ± 0.33	0.28 ± 0.33	0.499 ± 0.005
5084942	161.01	p	2.28	0.85	1.04	-0.14 ± 0.35	-0.31 ± 0.32	0.05 ± 0.35	0.502 ± 0.010
5115978	823.01	n	0.70	1.05	1.09	-0.01 ± 0.22	0.22 ± 0.21	-0.51 ± 0.17	0.501 ± 0.002
5283458	1547.01	c	1.10	1.77	0.97	-0.89 ± 0.14	0.78 ± 0.28	-0.41 ± 0.59	0.514 ± 0.007
5357901	188.01	p!	0.27	0.35	0.39	0.46 ± 0.28	-0.04 ± 0.35	-0.35 ± 0.31	0.499 ± 0.001
5358624	830.01	p!	0.66	0.30	0.51	-0.00 ± 0.32	-0.20 ± 0.30	-0.09 ± 0.31	0.501 ± 0.002
5383248	261.01	p!	3.91	0.96	0.35	-0.83 ± 0.18	0.56 ± 0.40	-0.89 ± 0.12	0.497 ± 0.012
5651104	840.01	p?	0.35	0.70	0.84	0.09 ± 0.35	0.12 ± 0.35	0.37 ± 0.31	0.501 ± 0.003
5683743	412.01	p	4.23	1.08	1.00	-0.03 ± 0.33	0.26 ± 0.31	-0.63 ± 0.20	0.496 ± 0.010
5728139	206.01	p!	6.84	2.67	1.62	0.06 ± 0.26	-0.48 ± 0.20	0.34 ± 0.23	0.503 ± 0.007
5780885	97.01	p!	1.49	0.68	1.09	0.10 ± 0.26	0.18 ± 0.25	-0.20 ± 0.25	0.500 ± 0.002
5794240	254.01	p!	0.42	0.35	0.24	0.39 ± 0.28	-0.34 ± 0.29	0.08 ± 0.33	0.501 ± 0.002
5812701	12.01	p!	9.47	1.99	1.98	0.23 ± 0.39	-0.01 ± 0.41	-0.37 ± 0.35	0.485 ± 0.011
6046540	200.01	p!	1.60	0.43	0.49	-0.33 ± 0.40	0.60 ± 0.29	0.30 ± 0.41	0.501 ± 0.005
6061119	846.01	p	0.53	2.37	1.41	0.24 ± 0.55	0.42 ± 0.48	0.28 ± 0.53	0.501 ± 0.004
6291653	850.01	p	1.05	0.90	1.03	-0.48 ± 0.31	-0.24 ± 0.38	-0.30 ± 0.37	0.504 ± 0.005
6300348	212.01	c	4.34	0.66	1.23	-0.51 ± 0.28	-0.28 ± 0.35	0.36 ± 0.33	0.513 ± 0.010
6309763	611.01	c	0.26	0.60	0.39	-0.13 ± 0.40	-0.17 ± 0.40	0.78 ± 0.16	0.500 ± 0.003
6522242	855.01	p	1.34	1.04	1.90	-0.71 ± 0.22	0.80 ± 0.16	-0.60 ± 0.29	0.501 ± 0.002
6526710	856.01	c	0.94	2.93	2.91	-0.38 ± 0.30	0.11 ± 0.35	-0.48 ± 0.27	0.498 ± 0.002
6634112	5308.01	c?	0.09	0.18	0.39	0.04 ± 0.58	-0.49 ± 0.44	0.41 ± 0.48	0.501 ± 0.001
6842345	6774.01	n	0.20	0.83	0.53	-0.32 ± 0.45	-0.01 ± 0.50	0.10 ± 0.49	0.502 ± 0.002
6849046	201.01	p	0.44	1.00	1.03	0.09 ± 0.33	-0.19 ± 0.32	-0.89 ± 0.07	0.503 ± 0.001
6922244	10.01	p!	0.99	0.98	0.53	0.37 ± 0.24	-0.21 ± 0.27	0.20 ± 0.27	0.498 ± 0.002
7046804	205.01	p	0.90	1.17	0.36	0.38 ± 0.32	0.28 ± 0.35	-0.11 ± 0.37	0.499 ± 0.002
7051180	64.01	c?	1.98	0.33	0.52	0.36 ± 0.25	0.62 ± 0.18	0.37 ± 0.25	0.496 ± 0.006
7380537	883.01	c	0.31	0.31	0.31	-0.06 ± 0.32	0.09 ± 0.31	-0.52 ± 0.23	0.497 ± 0.001
7529266	680.01	p!	7.07	1.17	1.90	-0.20 ± 0.25	0.38 ± 0.22	-0.11 ± 0.26	0.498 ± 0.004
7778437	131.01	p	2.90	0.96	1.12	-0.04 ± 0.28	0.43 ± 0.23	-0.46 ± 0.22	0.499 ± 0.004
7832356	1456.01	p	59.7	3.07	3.22	-0.50 ± 0.27	-0.72 ± 0.17	0.77 ± 0.14	0.580 ± 0.092
7849854	897.01	p	0.68	0.61	0.51	-0.07 ± 0.27	-0.12 ± 0.26	-0.11 ± 0.26	0.502 ± 0.002
7877496	202.01	p!*	0.52	0.38	0.32	0.26 ± 0.23	0.37 ± 0.22	-0.07 ± 0.25	0.501 ± 0.001
7950644	192.01	p!	0.96	1.27	0.88	0.29 ± 0.28	0.27 ± 0.28	-0.47 ± 0.23	0.499 ± 0.001
8039892	903.01	p?	9.76	1.41	1.20	0.15 ± 0.28	0.13 ± 0.28	0.36 ± 0.25	0.520 ± 0.014
8191672	18.01	p!*	1.44	1.18	1.60	-0.09 ± 0.24	0.20 ± 0.23	-0.73 ± 0.11	0.501 ± 0.002
8255887	908.01	p	1.72	0.69	0.74	-0.45 ± 0.27	-0.35 ± 0.29	0.11 ± 0.33	0.496 ± 0.004
8260218	1066.01	c	4.77	0.82	1.27	-0.02 ± 0.41	-0.46 ± 0.32	0.48 ± 0.31	0.482 ± 0.014
8349582	122.01	p!	8.66	1.41	1.13	0.29 ± 0.46	0.60 ± 0.32	0.61 ± 0.31	0.500 ± 0.021
8359498	127.01	p!	0.71	0.73	0.89	0.23 ± 0.29	-0.04 ± 0.30	-0.70 ± 0.15	0.498 ± 0.002
8544996	913.01	p	0.55	1.40	0.75	0.35 ± 0.28	-0.13 ± 0.31	-0.51 ± 0.24	0.499 ± 0.001
8684730	319.01	c	9.60	4.73	4.51	-0.22 ± 0.36	-0.14 ± 0.37	0.02 ± 0.38	0.497 ± 0.015
8711794	105.01	p	2.65	1.64	0.44	0.54 ± 0.50	-1.00 ± 0.00	-0.51 ± 0.52	0.488 ± 0.016
8866102	42.01	p	5.10	1.87	1.98	-0.25 ± 0.54	0.85 ± 0.16	0.24 ± 0.54	0.531 ± 0.012

**Notes.** <sup>(a)</sup>Identification number of the host star in the *Kepler* Input Catalog (Kepler Mission Team 2009). <sup>(b)</sup>Number of the KOI. <sup>(c)</sup>Averaged over all time-windows. The values of  $r_{ms}$ ,  $r_{me}$ ,  $r_{se}$ , and  $\langle A_s \rangle$  are given with their standard deviation margins. <sup>(d)</sup>Status marks: p – confirmed planet; c – candidate (i.e., no confirmation yet); n – probably non-planet, i.e., object with false-positive status or unrealistic radius (see clarifications in the related text); extensions: ! – confirmed exoplanet with an estimated mass  $< 13 M_J$ ; ? – previously suggested, but canceled false-positive status or stellar eclipses; \* – confirmed status and the measured planetary mass values, but with stellar eclipse flag in *Kepler* data.

Table A.1. continued.

KIC <sup>(a)</sup>	KOI <sup>(b)</sup>	Status	$\sigma_m$ 10 <sup>-3</sup> days	$\sigma_s$ 10 <sup>-3</sup> days	$\sigma_e$ 10 <sup>-3</sup> days	$r_{ms}$	$r_{me}$	$r_{se}$	$\langle A_s \rangle$
9115800	421.01	p	0.76	0.98	0.90	0.45 ± 0.40	0.10 ± 0.50	0.00 ± 0.50	0.499 ± 0.003
9166862	931.01	p	1.01	0.86	0.69	-0.00 ± 0.30	0.58 ± 0.20	-0.40 ± 0.25	0.499 ± 0.002
9305831	204.01	p!	1.92	0.74	0.72	0.36 ± 0.24	-0.13 ± 0.27	-0.71 ± 0.14	0.503 ± 0.004
9410930	196.01	p!	0.58	0.56	0.39	-0.11 ± 0.23	0.03 ± 0.24	0.42 ± 0.19	0.501 ± 0.001
9595827	217.01	p	1.40	0.22	0.58	-0.39 ± 0.27	-0.28 ± 0.29	0.14 ± 0.31	0.504 ± 0.004
9631995	22.01	p!	0.63	1.51	1.53	-0.54 ± 0.27	0.25 ± 0.35	-0.62 ± 0.23	0.502 ± 0.002
9643874	1457.01	p	2.54	0.67	1.01	-0.62 ± 0.31	0.77 ± 0.21	-0.41 ± 0.42	0.499 ± 0.008
9651668	183.01	p!	0.41	0.35	0.40	-0.16 ± 0.26	0.34 ± 0.24	-0.28 ± 0.25	0.501 ± 0.001
9941662	13.01	p!*	0.41	0.55	0.43	0.18 ± 0.19	0.02 ± 0.20	-0.55 ± 0.14	0.477 ± 0.001
9962595	5745.01	c?	0.08	0.74	0.40	0.47 ± 0.35	0.09 ± 0.44	0.55 ± 0.31	0.500 ± 0.002
10158418	1784.01	c	0.11	0.79	1.11	1.00 ± 0.00	0.89 ± 0.12	0.88 ± 0.13	0.503 ± 0.006
10264660	98.01	p!	3.06	1.14	0.50	-0.73 ± 0.14	-0.14 ± 0.28	0.21 ± 0.28	0.501 ± 0.004
10272640	1074.01	p	4.83	0.93	0.84	-0.57 ± 0.20	-0.16 ± 0.29	-0.12 ± 0.30	0.491 ± 0.009
10295951	1154.01	n	2.95	4.08	2.10	0.83 ± 0.09	-0.76 ± 0.12	-0.81 ± 0.10	0.497 ± 0.002
10318874	104.01	p!	0.92	0.64	0.40	-0.10 ± 0.40	0.57 ± 0.28	-0.77 ± 0.16	0.502 ± 0.006
10395543	531.01	c	0.22	0.37	0.28	0.29 ± 0.46	0.58 ± 0.33	-0.54 ± 0.36	0.506 ± 0.001
10418224	428.01	p!	18.8	1.67	0.95	-0.40 ± 0.27	0.23 ± 0.30	-0.62 ± 0.19	0.489 ± 0.018
10619192	203.01	p!	0.58	0.26	0.25	-0.10 ± 0.23	-0.31 ± 0.21	0.01 ± 0.24	0.502 ± 0.001
10666592	2.01	p!	0.70	0.32	0.41	-0.10 ± 0.20	-0.06 ± 0.20	-0.19 ± 0.19	0.504 ± 0.001
10748390	3.01	p!	1.24	0.74	0.44	0.59 ± 0.25	0.05 ± 0.38	-0.02 ± 0.38	0.482 ± 0.003
10874614	17.01	p!	0.50	0.84	1.47	-0.59 ± 0.18	0.18 ± 0.26	-0.56 ± 0.18	0.499 ± 0.002
10904857	194.01	p?	0.48	0.45	0.29	0.29 ± 0.30	0.50 ± 0.25	0.08 ± 0.33	0.501 ± 0.001
11046458	214.01	p!	0.30	0.42	0.73	0.63 ± 0.25	0.12 ± 0.40	-0.27 ± 0.38	0.499 ± 0.002
11138155	760.01	c	0.83	0.72	0.54	0.73 ± 0.19	0.87 ± 0.10	0.64 ± 0.24	0.501 ± 0.002
11180361	971.01	n	2.78	2.37	2.59	0.20 ± 0.15	0.40 ± 0.13	-0.57 ± 0.11	0.494 ± 0.004
11359879	128.01	p!	0.83	0.54	0.63	-0.04 ± 0.33	0.55 ± 0.23	-0.36 ± 0.29	0.503 ± 0.002
11391018	189.01	p	0.74	3.24	3.12	-0.89 ± 0.10	0.64 ± 0.26	-0.75 ± 0.20	0.504 ± 0.003
11404644	6085.01	n	2.23	1.05	1.00	-0.26 ± 0.27	0.12 ± 0.28	-0.82 ± 0.10	0.502 ± 0.003
11414511	767.01	p	0.71	0.52	0.56	-0.47 ± 0.23	-0.38 ± 0.25	-0.32 ± 0.26	0.503 ± 0.002
11446443	1.01	p!	0.08	0.23	0.25	0.37 ± 0.29	0.01 ± 0.33	-0.27 ± 0.31	0.500 ± 0.001
11449844	125.01	n	2.96	0.81	0.47	0.25 ± 0.54	0.36 ± 0.50	0.77 ± 0.24	0.493 ± 0.006
11502867	195.01	p!	0.43	0.41	0.34	0.15 ± 0.33	-0.05 ± 0.33	0.55 ± 0.23	0.499 ± 0.002
11517719	1416.01	n	3.84	1.42	1.52	-0.19 ± 0.20	-0.05 ± 0.20	-0.51 ± 0.15	0.501 ± 0.004
11554435	63.01	p!	3.46	0.40	0.49	-0.59 ± 0.32	-0.45 ± 0.40	0.77 ± 0.20	0.518 ± 0.012
11804465	20.01	p!	1.64	1.69	1.25	-0.66 ± 0.16	0.74 ± 0.12	-0.93 ± 0.04	0.502 ± 0.002
11853905	7.01	p!	5.73	0.95	0.73	0.00 ± 0.35	-0.22 ± 0.34	0.04 ± 0.35	0.481 ± 0.011
12019440	186.01	p	1.09	0.88	1.01	-0.09 ± 0.27	0.20 ± 0.27	-0.89 ± 0.06	0.499 ± 0.002
12105051	141.01	c	0.65	0.41	0.32	-0.26 ± 0.35	-0.23 ± 0.36	0.87 ± 0.09	0.500 ± 0.004
12251650	621.01	c?	0.14	0.36	0.54	0.16 ± 0.40	0.06 ± 0.41	0.36 ± 0.35	0.503 ± 0.001
12403119	1478.01	p	3.45	6.68	7.26	-	0.509 ± 0.00	-	0.509 ± 0.006
12557548	3794.01	p	1.51	2.00	2.12	-0.41 ± 0.20	0.43 ± 0.20	-0.82 ± 0.08	0.484 ± 0.006

Table A.2. Best examples of KOIs with a varying transit borders timing.

KIC	KOI	Status	$\frac{\sigma_s}{\epsilon_s}$	$\frac{\sigma_e}{\epsilon_e}$	$\frac{r_{se}}{\sigma_{rse}}$	$r_{se}$	$N_w$	$R_p$	$a_p$
								Earth's radii	
								a.u.	
3749365	1176.01	p	0.94	0.97	3.31	-0.61 ± 0.18	13	8.78	0.025
5115978	823.01	n	1.36	1.39	3.05	-0.51 ± 0.17	19	72.7	0.020
5683743	412.01	p	1.10	0.98	3.11	-0.63 ± 0.20	10	7.31	0.050
6849046	201.01	p	2.22	2.46	12.5	-0.89 ± 0.07	10	9.00	0.052
8191672	18.01	p!*	2.40	3.17	6.48	-0.73 ± 0.11	18	14.9	0.050
8359498	127.01	p!	1.67	2.48	4.58	-0.70 ± 0.15	12	10.4	0.045
8544996	913.01	p	2.82	1.61	2.16	-0.51 ± 0.24	11	10.5	0.048
9305831	204.01	p!	1.05	0.98	5.11	-0.71 ± 0.14	14	12.4	0.044
9941662	13.01	p!*	1.63	1.47	3.93	-0.55 ± 0.14	26	21.4	0.039
10295951	1154.01	n	4.47	2.76	8.41	-0.81 ± 0.10	12	26.0	0.080
10874614	17.01	p!	1.93	2.91	3.06	-0.56 ± 0.18	14	13.0	0.044
11180361	971.01	n	1.39	1.37	5.37	-0.57 ± 0.11	36	133.	0.017
11404644	6085.01	n	1.23	1.51	8.47	-0.82 ± 0.10	13	25.8	0.065
11517719	1416.01	n	1.52	2.01	3.35	-0.51 ± 0.15	25	15.7	0.036
11804465	20.01	p!	2.86	2.39	26.5	-0.93 ± 0.04	13	18.0	0.055
12019440	186.01	p	1.74	2.21	16.0	-0.89 ± 0.06	14	12.9	0.043
12557548	3794.01	p	1.90	1.68	10.1	-0.82 ± 0.08	18	22.9	0.013